Ciliberti and Nicolosi
Advances in Aerodynamics (2025) 7:3
https://doi.org/10.1186/s42774-024-00189-x

Advances in Aerodynamics

RESEARCH Open Access

Lateral-directional wind tunnel tests of the PROSIB 19-pax aircraft model

Danilo Ciliberti[1*] and Fabrizio Nicolosi[1]

*Correspondence:
danilo.ciliberti@unina.it

[1] Department of Industrial Engineering, University of Naples Federico II, Naples 80125, Italy

Abstract

This paper presents the power-off, lateral-directional wind tunnel tests on the fixed-wing, 19-passenger aircraft model developed within the Italian PROSIB project. The concept is an innovative small air transport airplane with distributed propellers and hybrid-electric powerplant. By measuring the aerodynamic forces and moments, the experimental investigation focused on the estimation of the power-off stability and control derivatives, highlighting the effects of the aerodynamic interference. Tests included a belly-mounted pod, simulating a battery storage unit, and two distinct empennage configurations: a body-mounted (low) horizontal tail and a T-tail (high). Numerical analyses were also used to further highlight the role of aerodynamic interference in the generation of forces and moments. For instance, wind tunnel data have shown a beneficial effect of the belly pod on the aircraft directional stability (+13%), but were in contrast with the results of numerical analyses (−30%). The measured sidewash depends also from the empennage layout, not only from the vertical tail planform area. Simulations confirmed an excessive directional stability with respect to the directional control in the ratio of 1.65, suggesting that such class of airplane should have a larger rudder chord ratio or a horn balance. Combined tests at different angles of attack and flap deflections revealed some issues on the lateral stability of the model, which are related to the velocity circulation on the wing in high-lift conditions counteracting the effective dihedral of the model's layout. The collected dataset of aerodynamic derivatives will serve as reference for a next experimental investigation on the aero-propulsive effects and provide useful information to researchers and professionals involved in similar design studies.

Keywords: Experimental aerodynamics, Wind tunnel testing, Stability and control, Sidewash, Small air transport

1 Introduction

The pursuit of energy efficiency air transport to limit the aviation impact to climate change [1] has promoted widespread research in hybrid and electric propulsion aircraft [2–5]. At this scope, the Italian PROSIB project was aimed at developing innovative aircraft configurations with hybrid-electric propulsion systems. PROSIB was the first Italian project that addresses integrated feasibility studies and the deployment of distributed hybrid/electric propulsion technology, promoting the development of the national ecosystem ready to contribute to the technological development activities envisaged in

H2020 and FP9. Started in 2018 and concluded in 2021, it had the primary objective to achieve a 20% reduction in the energy consumption of regional air transport with respect to conventional propulsion solutions existing in year 2000. The project investigated configurations for regional aircraft and rotary wing platform and architectures for propulsion systems including distributed hybrid/electric technologies to identify the best strategy to use the different on-board energy sources. Configuration studies have been supported by trend analysis of the main enabling technologies and their preliminary validation through wind tunnel and lab tests. As concerns the authors' contributions to the project, there were the assessment of technological requirements necessary for the "electrification" of an ATR-42 class aircraft, associated critical issues and sensible roadmap [6], as well as the development of innovative configurations for both 40- and 19-passenger platforms [7].

This paper deals with the lateral-directional wind tunnel testing of a new 19-passenger airplane model [6, 8], representative of the Small Air Transport (SAT) category defined in the FlightPath 2050 and ACARE documents [9, 10]. Although the global impact of the emissions of such category is small, it is believed that the implementation of new technologies on the SAT segment will work as a bridge between experimental aircraft and full-scale commercial aviation. In fact, SATs offer a feasible platform for demonstrating innovative technologies more effectively than larger passenger aircraft, due to reduced operative costs. For instance, alternative propulsion systems, initially introduced in light aircraft, have attracted significant attention in recent years. As such, the SAT segment serves as an ideal platform to test innovative aircraft systems, establishing best practices, and laying technological roadmaps for larger aircraft demonstrators [11].

The wind tunnel is the primary experimental method to estimate the aircraft stability and control characteristics since the dawn of aviation. Methods reported in manuals and textbooks [12–14] were developed from the collection of a huge amount of wind tunnel data on aircraft components and configurations. Some of these reports focused on a specific aircraft or technique [15–17], while others investigated the effects of component installation on static stability [18–23] or presented advice on test procedures, including propulsive effects [24]. The second type of reports is of particular interest for aircraft designers and analysts dealing with a large number of concept alternatives in preliminary design phases. Moreover, since full-scale testing is often infeasible, numerous experiments focused on the aerodynamic interactions between scaled models and wind tunnel boundaries helped engineers to establish procedures to correct and eventually extrapolate wind tunnel data to free-flight conditions [25, 26]. The wind tunnel is, nowadays, also used to present test cases to the research community to validate numerical methods [27–29], which will never completely replace the experimental approach, but rather support its development and execution.

The aircraft model investigated in this work has a removable appendix installed below the fuselage, simulating a battery storage unit. The effects of external storage on the aircraft aerodynamics and static stability were investigated by several authors, especially on high-speed fighter aircraft [30–32]. The experiments were focused on the best position of an external pylon-mounted pod on either the wing or the fuselage. To the authors' best knowledge, there are few available data on the effects of pods integrated within the fuselage belly, although such an arrangement is not unusual in hybrid-electric aircraft concepts, like the Heart Aerospace ES-30 [33] or the Ampaire Eco Caravan [34], as well as in conventional designs like the Cessna 208 Grand Caravan. A patent for a removable cargo pod for light aircraft was obtained by Shelton [35] in 2009. That document reports claims as easy installation and removal, eliminating its weight and drag when not needed, but no useful data on the impact of the aircraft stability are presented. More recently, Moonan [36] investigated the aerodynamics of a belly storage for the NASA MAPIR project, which was installed below a Piper Navajo aircraft. The preliminary predictions performed with simplified numerical analyses were invalid as flight tests provided totally different data, thus the necessity of an experimental investigation on complex aerodynamic systems.

As concerns the aerodynamic interference of the wing-body on the empennage, many reports were focused on a specific aircraft, while a few others like [23] investigated different wing–tail arrangements. As concerns longitudinal stability, the concept of downwash is well known. A method for the estimation of the downwash gradient was developed by Silverstein and Katzoff [37] and expanded in the USAF DATCOM manual [13]. The approach provides a decreasing downwash gradient with the tail distance from the wing (both longitudinally and vertically), regardless of the tail blanketing due to the wing wake in some regions. This effect, particularly dangerous for aircraft with swept wings installed in the lower part of the fuselage and horizontal tailplanes mounted at height on the vertical tailplane, was highlighted by Spreemann [38].

Lateral-directional dynamics is usually more complicated because of the asymmetric flow involved. The effectiveness of a vertical tail — providing directional stability and control in sideslip — is dependent on a variety of factors arising from the mutual aerodynamic interference among the aircraft components. The wing-body interference on the tailplane in sideslip flow is known as sidewash [39]. Both the dynamic pressure and local angle of attack at the vertical tailplane are altered by the wing-body system, largely because of their relative vertical position and, in a lesser quantity, by the wing planform parameters. Sidewash can be measured by wake surveys or estimated from aerodynamic sideforce or yawing moment measurements [15, 19, 23, 39–43]. Although the vortex system developed in sideslip flow is more complicated to model than that of the longitudinal case, the relatively small dependence from the aircraft angle of attack and Mach number made it possible to develop an empirical method valid for subsonic flow [13]. Apart from the sidewash, body-tail (wing-off) combinations do alter the sideforce generated by the vertical tail because of the end-plate effect [15, 18–22, 27], which boosts the vertical tail lift gradient as its effective aspect ratio was larger.

This paper presents the second experimental test campaign on the PROSIB 19-passenger aircraft model [8] to evaluate its power-off lateral-directional stability and control characteristics. A rendering of the concept is shown in Fig. 1. Nacelle and propellers have not been investigated yet. A removable pod to simulate battery storage was installed below the fuselage. The full-scale storage would have a useful volume of about 4 m^3, 40% of which occupied by the battery with a mass of about 1500 kg, including casing, cables, and internal electronics. The remainder of the volume would be shared by the thermal and power management systems. Moreover, the project consortium required an experimental comparison between a body-mounted horizontal

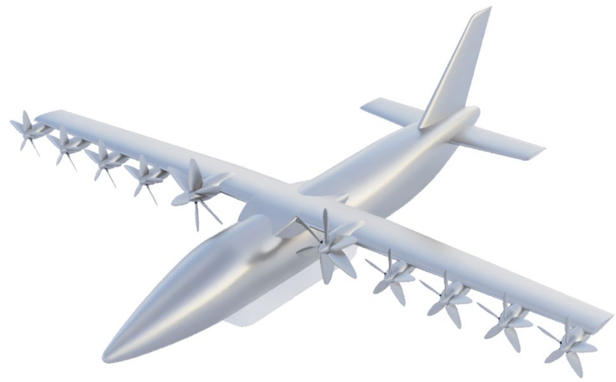

Fig. 1 Rendering of the PROSIB 19-pax concept

tail vs. a T-tail configuration. The latter was designed such to keep the same directional stability of the former [27, 44], but with a smaller vertical tail planform area and aspect ratio.

Therefore, the purpose of this paper is to characterize the lateral-directional stability and control of a generic model of hybrid-electric SAT aircraft with a conventional tube-and-wing layout. The objectives are here resumed:

- establish a dataset of power-off aerodynamic derivatives;
- compare two tailplanes to identify the best configuration layout;
- provide insights on the effect of the belly-mounted pod.

These will serve as reference for the powered wind tunnel tests to evaluate the aero-propulsive effects due to distributed propulsion. At the same time, researchers working on similar aircraft configurations can benchmark the characteristics of their concepts with the experimental data here presented.

The authors highlight that their work is focused on a model that is representative of the SAT category, not a specific aircraft. It may be argued that the preliminary design and analysis of any aircraft can be rapidly made with semi-empirical methods. However, it has already been shown by the authors [27] that such methods were derived from wind tunnel data on aircraft geometries quite different from today in-service airplanes and that different methods can lead to a large scatter in the evaluation of aerodynamic derivatives, even on a standard tube-and-wing configuration. Therefore, the authors are confident that this work will be a valuable source of data on the aerodynamic interference, stability and control characteristics of the 19-seater class, which is not directly represented in the publicly available semi-empirical methods. At this scope, a direct comparison between the conventional and T-tail empennage configurations, which are the most common layouts, has been made. Moreover, the aerodynamic interference data here presented on a belly pod integrated in the fuselage, which can be used as a cargo or energy storage, are missing in the public literature. Finally, the experimental investigation highlighted a combined effect of high-lift devices, sideslip angle, and angle of attack that is detrimental to lateral stability and, to the authors' best knowledge, is not clearly presented in literature. All these considerations and data will help enabling the SAT segment as a platform demonstrator for the next aviation technologies.

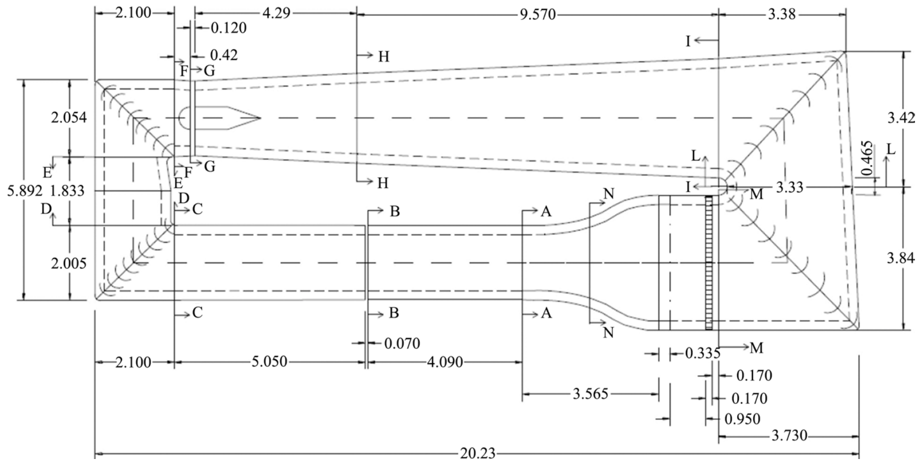

Fig. 2 Subsonic wind tunnel layout. Units in meters. Flow runs in clockwise direction

The remainder of the paper is structured as follows. Section 2 describes the wind tunnel facility, the instrumentation, the aircraft model, and the setup of the wind tunnel runs. Section 3 discusses the results of the tests, highlighting the effects of aerodynamic interference and providing an estimation of aircraft stability and control characteristics, with a focus on the influence of the pod and tail effectiveness in different configurations. Section 4 draws the conclusions of the work.

2 Wind tunnel setup

2.1 Experimental facility and equipment

The tests have been performed in the main subsonic wind tunnel facility of the Department of Industrial Engineering of the University of Naples "Federico II". It is a closed-return, closed-test section tunnel operating at subsonic speeds. The test section (segment A-B in Fig. 2) has a tempered rectangular shape of 2.0 m width and 1.4 m height. With a maximum power of about 150 kW, the flow speed in the test section can reach a value of 50 m/s. The average turbulence intensity at the test section inlet is 0.10%. The measurement equipment includes:

- lateral-directional strain gauge balance;
- wall-mounted pressure transducers;
- potentiometer measuring sideslip angle;
- temperature probe.

An internal strain-gauge balance, made in-house with 2024-T3 aluminum alloy, was used to measure the sideforce, yawing moment, and rolling moment. The accuracy and range of the measurement instruments are reported in Table 1. The directional attitude control was manually moved through a gear mechanism connected to a toothed wheel using a chain. This entire setup is located beneath the floor of the test chamber. Rotating the toothed wheel enabled the model to turn in the test section, thereby changing the sideslip angle.

2.2 Data acquisition system

The instrumentation for data acquisition and control included:

- A National Instruments USB-6341 device to acquire voltage signals from the sensors;
- A desktop PC with Windows 10 connected to the aforementioned device via USB;
- A LabVIEW virtual instrument to perform live measurements.

The virtual instrument was developed by the authors for the lateral-directional wind tunnel test campaign. The application established communication channels with the data acquisition board to get the analog signals of lateral-directional force and moments, angle of sideslip, temperature, and dynamic pressure.

To initialize the data acquisition process, a calibration matrix was loaded, along with parameters tailored to the aircraft model and wind tunnel characteristics. All the signals were acquired at a rate of 1000 Hz and averaged on 1000 samples. The measurements from the strain gauge balance and pressure transducers were taken with respect to a reference value, which was acquired at the start of each run with wind tunnel off. The potentiometer and temperature sensors had their internal calibration with their own reference voltage and did not need to be zeroed.

Standard aerodynamic coefficients have been used to normalize all aerodynamic forces. These coefficients were calculated based on reference parameters: the test section dynamic pressure q_∞, the wing span b, and the wing planform area S. The Reynolds number was determined with respect to the mean aerodynamic chord. At the flow speed of 20 m/s, the Reynolds number was about 430000. Wind tunnel corrections have been incorporated in the LabVIEW virtual instrument under the procedure outlined in the Appendix of a previous paper [8].

2.3 Aircraft model description

The aircraft experimental model was the same of Ref. [8]. It was entirely made in aluminum alloy by CNC manufacturing, except for the battery pod, which was made with ABS in additive manufacturing. A three-view drawing is provided in Fig. 3. The scale of the model was 1:15, with a wing planform area of 0.25 m^2 and a mean aerodynamic chord of 0.171 m. The airfoils were the NACA 23018 for the wing root and kink sections, the NACA 23015 for the wing tip section, and the NACA 0012 for the tailplane sections. The manufacturing and detailed design of the fittings were outsourced. The fuselage was sufficiently large to install the strain gauge balance inside. The tailplane group could be entirely removed from the fuselage.

Two tail configurations were realized: a body-mounted horizontal tail and a T-tail. The latter was designed with the VeDSC method [27] to provide the same directional stability of the former, exploiting the end-plate effect [20]. Under this assumption, the T-tail configuration was sized with about 13% less vertical tail planform area. The two configurations are compared in Fig. 4 and their differences are detailed in Table 2. The aerodynamics of the two empennage groups are discussed in the next sections. Figure 5 shows pictures of the aircraft model with the different tail configurations. Figure 6 shows an example of flap and rudder deflections.

Table 1 Instruments' range of measurement and accuracy

Instrument/axis	Full-scale output	Max error
Sideforce	±20 kgf	0.10%
Yawing moment	±20 kgf·m	0.10%
Rolling moment	±20 kgf·m	0.10%
Pressure transducer	2500 Pa	0.12%
Potentiometer	±20°	0.20%
Temperature sensor	−50° to 150°	±1.0°

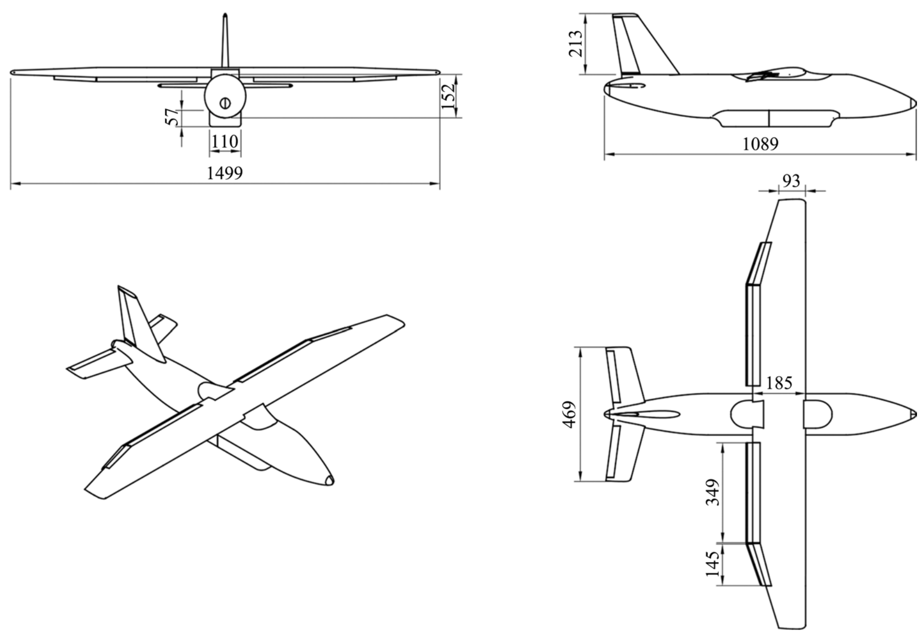

Fig. 3 Aircraft model drawings. Units in mm

2.4 Test matrix

The nomenclature indicating each aircraft model component is reported in Table 3. Each combination of symbols defines the buildup of aircraft components. Underscores separate the configuration layout from the movables deflection: flap and rudder. For instance, WBHVt_F15_R20 defines the configuration made up of wing, fuselage, horizontal and vertical planes in T-tail layout, with flap deflected by 15° and rudder deflected by 20°.

The list of the tested configurations is reported in Table 4. This is not the sequence of the tests, but rather a synoptic view of the combinations investigated. In each run, the model was rotated at different sideslip angles, but at constant angles of attack and movables deflection. The total number of tests was more than 80, including the effects of the angle of attack and the deflections of flaps and rudder. Preliminary tests were made to install trip strips to force the flow transition near the lifting surfaces' leading edges and to evaluate repeatability. These are not included in the table.

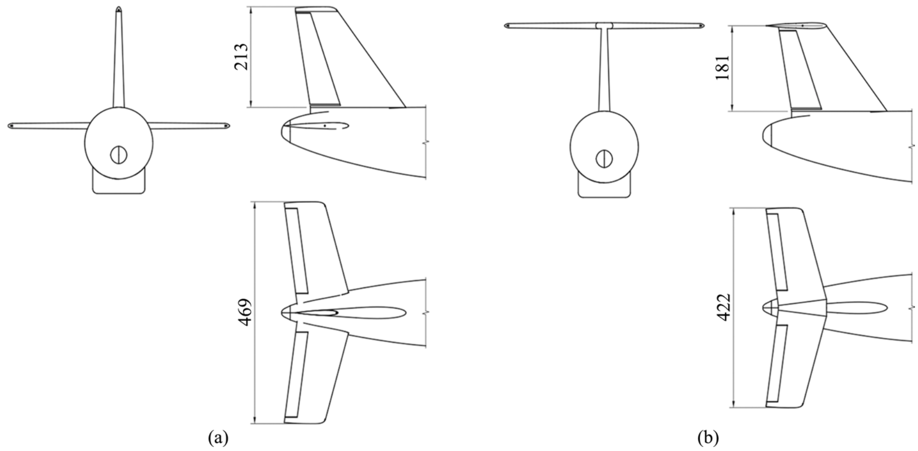

Fig. 4 Comparison of two tailplane configurations: **a** body-mounted; **b** T-tail. Units in mm

Table 2 Comparison of the two horizontal tailplanes' data

Parameter	Body-mounted	T-Tail
Root chord	123 mm	102 mm
Tip chord	87 mm	77 mm
Span	469 mm	422 mm
Leading edge sweep angle	15°	15°
Planform area	49 245 mm^2	37 769 mm^2
Aspect ratio	4.47	4.72
Taper ratio	0.71	0.75
Longitudinal distance from ref. point	560 mm	571 mm
Volume tail coefficient	0.645	0.505

3 Results and discussion

The scope of the wind tunnel runs was to acquire the lateral-directional force and moments in a variety of conditions. The results are here presented with the standard aerodynamic coefficients of sideforce C_Y, yawing moment $C_\mathcal{N}$, and rolling moment $C_\mathcal{L}$ vs. the sideslip angle β. To evaluate directional and lateral stabilities, the derivatives of the moment coefficients were estimated with a linear regression on the aerodynamic coefficients up to 8° of sideslip angle. The rudder control power was estimated as the leap between the curves with and without the rudder deflected, both at zero sideslip. Details will be given in the following sections. The adopted coordinate system is a body reference frame with the origin at the point P indicated in Fig. 7, which is at 25% chord length aft and 20% chord length below the wing root leading edge. With this coordinate system, the criteria for lateral-directional stability are:

$$C_{\mathcal{N}_\beta} > 0\,, \qquad C_{\mathcal{L}_\beta} < 0\,.$$

Repeatability tests have shown relative accuracy of the measurements of 1.2% for the C_Y, 2.4% for the $C_\mathcal{N}$, and 3.2% for the $C_\mathcal{L}$. It is here remarked that the longitudinal tests

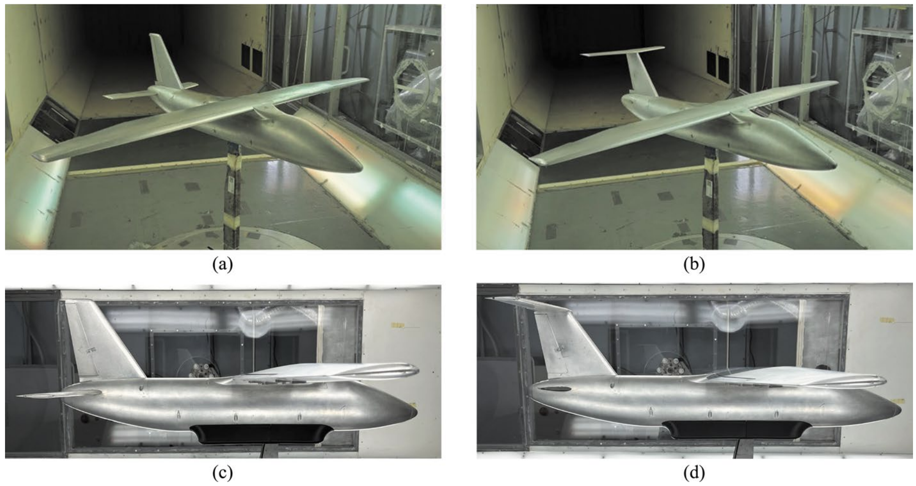

Fig. 5 The two tail configurations in the test section: **a** perspective of the body-mounted tail layout; **b** perspective of the T-tail layout; **c** side view of the body-mounted tail layout with pod; **d** side view of the T-tail layout with pod

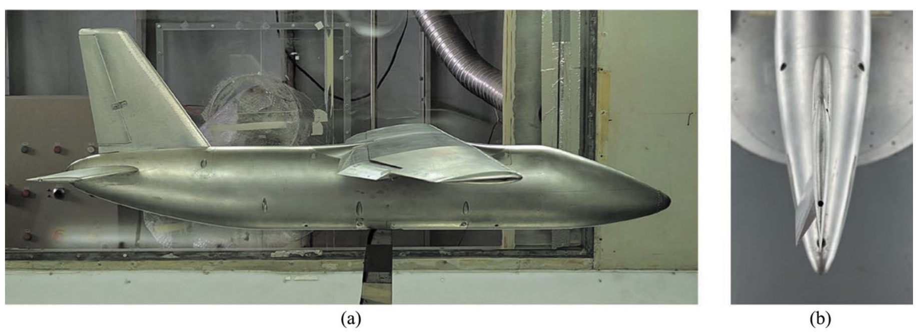

Fig. 6 Example of movables deflection: **a** flap; **b** rudder

with results on the lift, drag, and pitching moment coefficients were assessed by the authors in Ref. [8] and that those results will not be discussed here.

3.1 Body, wing-body and wing-body-pod combinations

These are the combinations with tail off. The effects of the flaps and angle of attack are not discussed in this section. The charts of sideforce, yawing moment, and rolling moment coefficients are reported in Fig. 8. As expected, the sideforce coefficient was negative for all the combinations at positive angles of sideslip, whereas the yawing moment coefficient was negative because the unstable directional behaviour of the tail-off configurations. Finally, the sign of the rolling moment coefficient was positive for the fuselage alone, whereas it was negative for the wing-body combinations, since the high-wing layout provided lateral stability. The addition of components has determined an increase of the magnitude of the sideforce curve slope C_{Y_β} by 66% from the body to the wing-body and by a further 84% to the wing-body-pod. Conversely, the addition of the wing and pod did not have a disruptive change of the directional stability derivative $C_{\mathcal{N}_\beta}$. The installation of the pod decreased the magnitude of wing-body $C_{\mathcal{N}_\beta}$ by 13%, while it was neutral for the lateral stability derivative $C_{\mathcal{L}_\beta}$. Table 5 reports the aerodynamic

Table 3 Nomenclature for aircraft components

Symbol	Description
W	Wing
B	Body (i.e., fuselage)
H	Horizontal tail
P	Battery pod
Vb	Vertical tail (for body-mounted horizontal)
Vt	Vertical tail (for T-tail horizontal)
_	Separator for movables
F	Flap
R	Rudder

Table 4 Test matrix. All the configurations were tested by sweeping the sideslip angle β

	Flap δ_f			Rudder δ_r			Angle of attack α	
Configuration	**0°**	**15°**	**30°**	**0°**	**±10°**	**±20°**	**0°**	**5°**
B							✓	✓
BVb				✓			✓	
BVt				✓			✓	
BHVb				✓			✓	✓
BHVt				✓			✓	✓
WB	✓	✓	✓				✓	✓
WBP	✓						✓	
WBVb	✓			✓			✓	
WBVt	✓			✓			✓	
WBHVb	✓	✓	✓	✓	✓	✓	✓	✓
WBHVt	✓	✓	✓	✓	✓	✓	✓	✓
WBPHVb	✓			✓			✓	
WBPHVt	✓			✓			✓	

A check mark indicates that the configuration was tested with those angle of attack, flap deflection, and rudder deflection, but not necessarily with a combination of them

derivatives for the investigated group. Further details on the effects of the pod are given in Section 3.4.

3.2 Effect of the tailplane on the wing-off combinations

By adding the vertical and horizontal tailplanes on the fuselage, the aerodynamic coefficients changed as shown in Fig. 9. The isolated body curves are reported for comparison. The vertical tailplane significantly increased the magnitude of all the aerodynamic coefficients, whereas the horizontal tailplane provided minor changes. The sideforce curve slope increased more than four times. Directional stability was introduced with the vertical tail, providing $C_{\mathcal{N}_\beta} = 0.0017$ deg^{-1} for the slender planform BVb and $C_{\mathcal{N}_\beta} = 0.0013$ deg^{-1} for the shorter planform BVt. The addition of the horizontal tail on the body did not alter the yawing moment coefficient derivative of the slender vertical tail (BHVb combination), whereas the installation of the top horizontal plane on the shorter vertical tail (BHVt combination) increased that derivative to the same value of the other tail. The

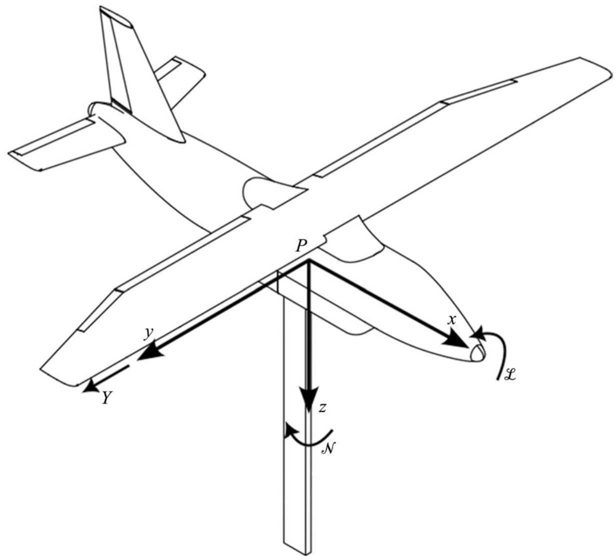

Fig. 7 Reference frame with indications on the positive sign of forces and moments

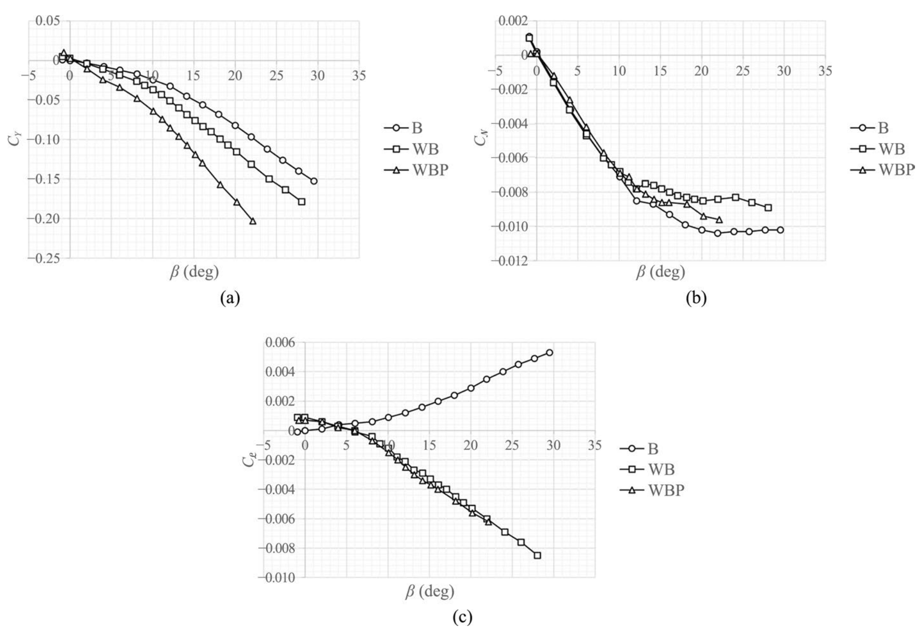

Fig. 8 Body, wing-body, and wing-body-pod combinations: **a** sideforce coefficient; **b** yawing moment coefficient; **c** rolling moment coefficient

application of the VeDSC method [27] to size the T-tail was fruitful. The smaller vertical planform of the T-tail configuration provided the same directional stability derivative of the larger and slender vertical tail with body-mounted horizontal plane.

At the same time, the tailplane group added lateral stability to the isolated body within a moderate range of sideslip angle, say up to 14°. With respect to the body-vertical (BV) configurations, the effect of the horizontal planes was to increase the magnitude of the lateral stability derivative $C_{\mathcal{L}_\beta}$ for the T-tail configuration (BHVt) and decrease it for the body-mounted configuration (BHVb). In particular, the BVt configuration had the lowest value of the lateral stability derivative, while the BHVt had the maximum value. Table 6 reports the aerodynamic derivatives for this investigation.

3.3 Effect of the wing-body on the tailplane

The high-wing plus body-tail combination, with or without the horizontal plane, is known to decrease the directional stability of the configuration [15, 18, 19, 23]. Test data have shown that the body-mounted tail had the strongest sideforce and yawing moment aerodynamic derivatives, whereas the T-tail significantly increased the rolling moment coefficient derivative, increasing the lateral stability derivative as highlighted in the previous section. The aerodynamic coefficients for the wing-on combinations, with and without tailplane, are shown in Fig. 10. Table 7 reports the aerodynamic derivatives for these configurations.

3.4 Effect of the pod

The belly-mounted pod was initially expected to slightly decrease the directional stability of the model, due to the larger side area. Instead, in Section 3.1 it was asserted that the pod provided a 13% reduction of wing-body directional instability. Given the model high-wing layout, it was reasonable to affirm that the effect of the pod was completely captured by the wing-body investigation. No further mutual aerodynamic interference could arise with tailplane. To validate this statement, the complete aircraft was investigated also with the pod installed. Results are reported in Fig. 11. The pod increased the slope of the sideforce curve by about 30%, the slope of the yawing moment curve by about 15%, and it did not affect the rolling moment curve. Directional and lateral stability on the complete aircraft model were affected with the same ratio of the wing-body.

The stabilizing effect of the pod on the wing-body directional motion was unexpected. Semi-empirical methods reported in [12, 13] do not account for protuberances of the fuselage cross-sections, and therefore they would not predict any change in wing-body directional stability due to the integrated belly pod located at a longitudinal station close to the fuselage center of mass. The strip method by Multhopp [45] would predict an increase of the instability of the fuselage alone, since that method is based on the sum of the square of the height of each strip in which the fuselage side view has been divided. The presence of the integrated belly pod, considered as an extension of the fuselage cross-section, would increase the local strips' height, increasing the magnitude of the $C_{\mathcal{N}_\beta}$.

To examine in depth the specific cause of the favorable contribution of the pod, numerical analyses were performed on the aircraft model in a steady, incompressible, fully-turbulent flow (Spalart-Allmaras model) with Simcenter STAR-CCM+. The mesh

Table 5 Tail-off stability derivatives. Units in deg^{-1}

Configuration	C_{Y_β}	$C_{\mathcal{N}_\beta}$	$C_{\mathcal{L}_\beta}$
B	−0.0021	−0.0008	0.00008
WB	−0.0035	−0.0008	−0.00015
WBP	−0.0064	−0.0007	−0.00015

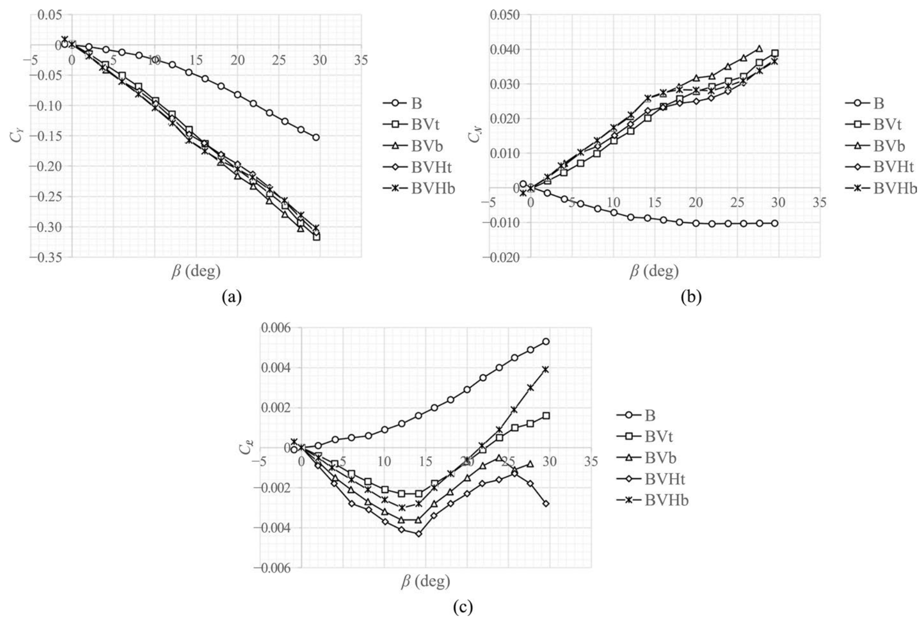

Fig. 9 Body, body-vertical, and body-horizontal-vertical combinations: **a** sideforce coefficient; **b** yawing moment coefficient; **c** rolling moment coefficient

was made up of about 8 to 11 million polyhedral cells (according to the investigated configuration) and 20 prism layers on the aircraft surfaces to account for the boundary layer. The mesh is shown in Fig. 12. Refinements were made on the wing-body junction and on sharp curvatures such as the edges of the lifting surfaces. The simulations were useful to evaluate those aerodynamic interference effects that were impossible to disclose with the wind tunnel balance only.

Wind tunnel data with and without tailplane were consistent, i.e., the directional stability in presence of the pod increased for all the tested combinations. Also, care was given on the installation of the pod to avoid contact with the support structure. However, the results of the numerical analyses gave an opposite trend. The application of the pod increased the magnitude of the yawing moment coefficient of the WB configuration by about 30%. Several runs were made to capture a possible effect of the support interference, which passed through the belly pod. Simulations were performed with the aircraft model in free-air with and without the model's support and also with the wind tunnel walls with and without the model's support. In all the cases, the presence of the sting did not significantly altered the value of the yawing moment coefficient (about 1%), while the presence of the wind tunnel walls increased this value by about 7%. This is in agreement with the wind tunnel corrections, where the measured dynamic pressure is increased by 9% due to wall effects.

Figure 13 shows a comparison between the pressure distribution (with respect to the reference value of 101325 Pa) for the WB and WBP configurations with both model support and tunnel walls simulated at $\beta = 6°$. The flow expansion on the downwind side of the pod is apparent. Therefore, there must be some interference effects that are not captured by the numerical analyses. Although wind tunnel data should validate the results of the numerical analyses and not vice versa, since the two methods gave opposite trends, it is better to avoid a definitive conclusion on the interference effect of the pod. Further investigations in the wind tunnel with a different system of measurements are needed.

3.5 Estimation of the sidewash effect

The aerodynamic interference of the wing-body on the tailplane in sideslip is known as sidewash effect, similarly to the downwash defined in the longitudinal plane. The sidewash effect is a measure of the effectiveness of the vertical stabilizer in generating sideforce or yawing moment, since the local sideslip angle in the region of the vertical tail is altered by the wing-body system. The angle of attack of the vertical surface is not β as it was undisturbed, but rather $\beta - \sigma$, with σ being the sidewash angle. It has been shown that the quantity of interest for the directional stability evaluation is the sidewash gradient $\mathrm{d}\sigma/\mathrm{d}\beta$ [15, 23]. The measurement of the sidewash gradient in the wind tunnel can be done analogously as the downwash case [8, 23], by combining the aerodynamic derivatives of sideforce [23] or yawing moment coefficients [15] measured on different configurations with and without horizontal tail. The formulations are similar:

$$\frac{q_\mathrm{V}}{q_\infty}\left(1-\frac{\mathrm{d}\sigma}{\mathrm{d}\beta}\right)=\frac{\overbrace{C_{Y_{\beta,\mathrm{WBV}}}-C_{Y_{\beta,\mathrm{WB}}}}^{\left(C_{Y_{\beta,\mathrm{V}}}\right)_\mathrm{WBV}}}{\underbrace{C_{Y_{\beta,\mathrm{BV}}}-C_{Y_{\beta,\mathrm{B}}}}_{\left(C_{Y_{\beta,\mathrm{V}}}\right)_\mathrm{BV}}}; \tag{1}$$

$$\frac{q_\mathrm{V}}{q_\infty}\left(1-\frac{\mathrm{d}\sigma}{\mathrm{d}\beta}\right)=\frac{\overbrace{C_{Y_{\beta,\mathrm{WBHV}}}-C_{Y_{\beta,\mathrm{WB}}}}^{\left(C_{Y_{\beta,\mathrm{V}}}\right)_\mathrm{WBHV}}}{\underbrace{C_{Y_{\beta,\mathrm{BHV}}}-C_{Y_{\beta,\mathrm{B}}}}_{\left(C_{Y_{\beta,\mathrm{V}}}\right)_\mathrm{BHV}}}; \tag{2}$$

$$\frac{q_\mathrm{V}}{q_\infty}\left(1-\frac{\mathrm{d}\sigma}{\mathrm{d}\beta}\right)=\frac{\overbrace{C_{\mathcal{N}_{\beta,\mathrm{WBV}}}-C_{\mathcal{N}_{\beta,\mathrm{WB}}}}^{\left(C_{\mathcal{N}_{\beta,\mathrm{V}}}\right)_\mathrm{WBV}}}{\underbrace{C_{\mathcal{N}_{\beta,\mathrm{BV}}}-C_{\mathcal{N}_{\beta,\mathrm{B}}}}_{\left(C_{\mathcal{N}_{\beta,\mathrm{V}}}\right)_\mathrm{BV}}}; \tag{3}$$

Table 6 Wing-off stability derivatives. Units in deg^{-1}

Configuration	C_{Y_β}	$C_{\mathcal{N}_\beta}$	$C_{\mathcal{L}_\beta}$
B	−0.0021	−0.0008	0.00008
BVb	−0.0102	0.0017	−0.00034
BVt	−0.0088	0.0013	−0.00022
BHVb	−0.0101	0.0017	−0.00027
BHVt	−0.0101	0.0017	−0.00046

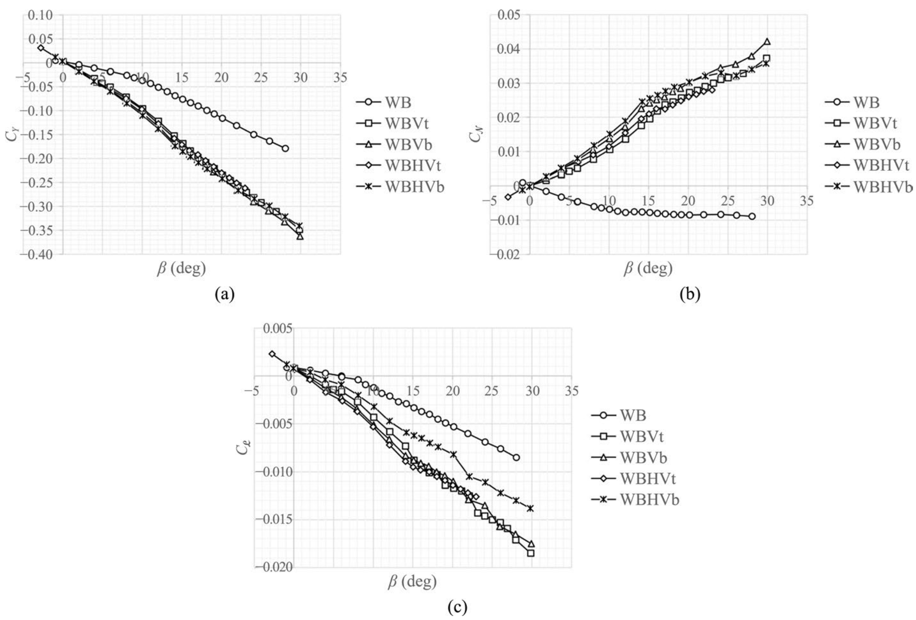

Fig. 10 Wing-body-tail combinations: **a** sideforce coefficient; **b** yawing moment coefficient; **c** rolling moment coefficient

$$\frac{q_{\mathrm{V}}}{q_{\infty}}\left(1-\frac{\mathrm{d}\sigma}{\mathrm{d}\beta}\right)=\frac{\overbrace{C_{\mathcal{N}_{\beta,\mathrm{WBHV}}}-C_{\mathcal{N}_{\beta,\mathrm{WB}}}}^{\left(C_{\mathcal{N}_{\beta,\mathrm{V}}}\right)_{\mathrm{WBHV}}}}{\underbrace{C_{\mathcal{N}_{\beta,\mathrm{BHV}}}-C_{\mathcal{N}_{\beta,\mathrm{B}}}}_{\left(C_{\mathcal{N}_{\beta,\mathrm{V}}}\right)_{\mathrm{BHV}}}}; \tag{4}$$

where Eqs. (1) and (2) are the estimation of the vertical tail effectiveness in sideslip on the sideforce without and with the horizontal tail, respectively, whereas Eqs. (3) and (4) are similar expressions based on the yawing moment coefficient derivatives. The ratio $q_{\mathrm{V}}/q_{\infty}$ is the dynamic pressure ratio at the vertical tail, which cannot be directly measured without a dedicated probe. The application of the above formulas gave the results reported in Table 8. All these wind tunnel runs were made at an angle of attack $\alpha=0°$. The effectiveness of the vertical surface was slightly larger for the smaller vertical tail without horizontal plane (Vt configuration). This is in contrast with the method reported in [13], where the effectiveness of the vertical tail in sideslip increases with its planform area and does not depend from the presence of the horizontal tail. Conversely, the installation of the horizontal surface made the body-mounted configuration Vb

Table 7 Wing-body-tail stability derivatives. Units in deg^{-1}

Configuration	C_{Y_β}	$C_{\mathcal{N}_\beta}$	$C_{\mathcal{L}_\beta}$
WB	−0.0035	−0.0008	−0.00015
WBVb	−0.0103	0.0013	−0.00051
WBVt	−0.0093	0.0009	−0.00043
WBHVb	−0.0104	0.0013	−0.00030
WBHVt	−0.0100	0.0012	−0.00058

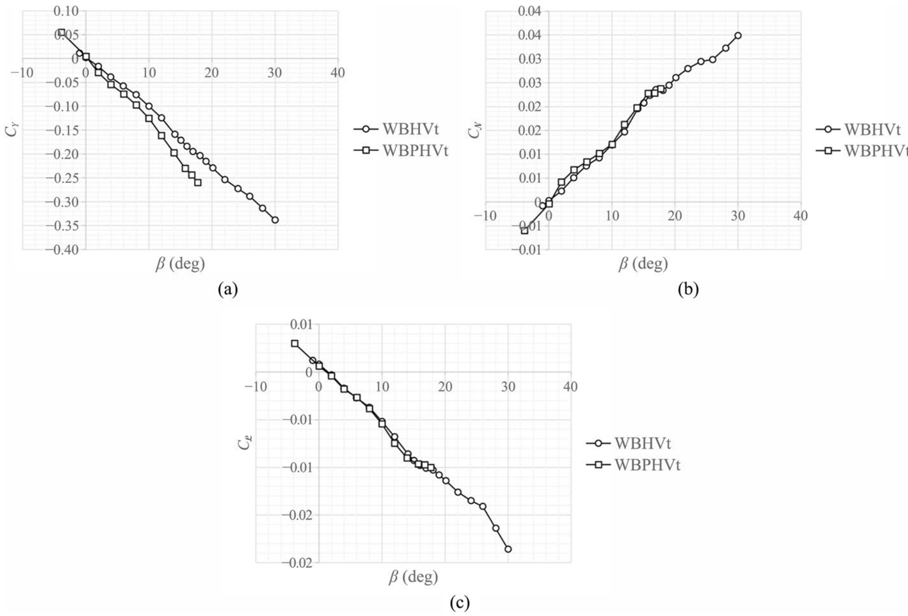

Fig. 11 Effect of the pod on the complete aircraft: **a** sideforce coefficient; **b** yawing moment coefficient; **c** rolling moment coefficient

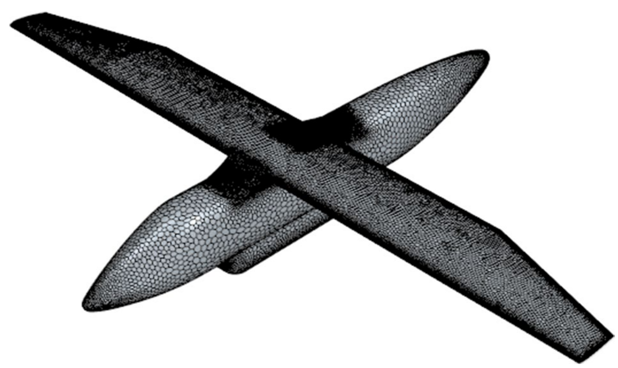

Fig. 12 The mesh on the WBP configuration for the numerical analyses

more effective than the T-tail layout. This was attributed to a stronger body-tail end-plate effect, whereas the sidewash angle induced by the wing-body system should be the same for both configurations. The sidewash gradient $\mathrm{d}\sigma/\mathrm{d}\beta$, which is with good approximation the complement to one of the vertical tail effectiveness in sideslip estimated with Eqs. (1) to (4), is about 0.15 for all the combinations.

The effect of sidewash is illustrated in Fig. 14, where numerical analyses allowed the illustration of the velocity vectors in two planes at the wing and the vertical tail. The WBHVb and the BHVb configurations at $\beta = 6°$ are compared. The induction of the wingtip vortex on the vertical tail flow field is apparent. The flowfield at the vertical tail is curved downstream due to the wing-body sidewash.

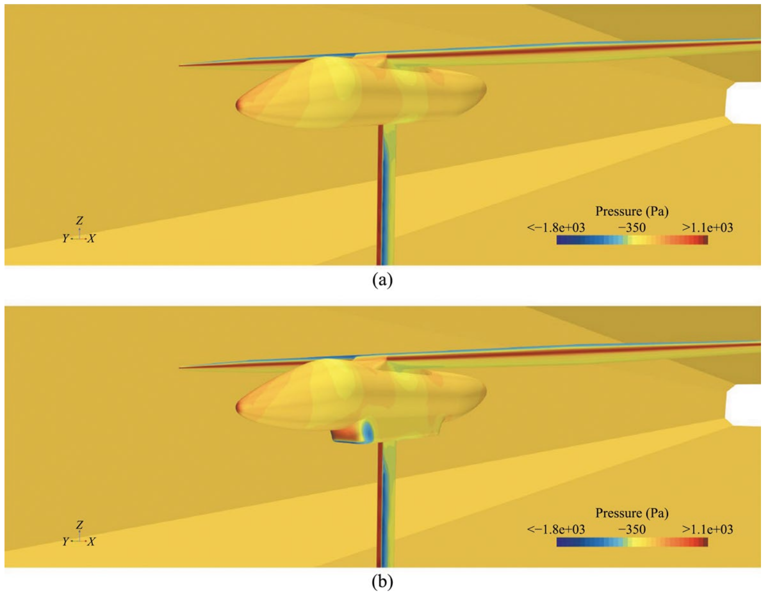

Fig. 13 Pressure distribution on the wing-body configuration simulated with the wind tunnel walls at $\beta = 6°$: **a** without pod; **b** with pod

3.6 Estimation of rudder control power

The evaluation of rudder control power was made with the difference between the aerodynamic curves with and without the rudder deflected, both at zero sideslip:

$$C_{\mathcal{N}_{\delta_\mathrm{r}}} = \frac{C_{\mathcal{N}}(\beta = 0°, \delta_\mathrm{r}) - C_{\mathcal{N}}(\beta = \delta_\mathrm{r} = 0°)}{\delta_\mathrm{r}} . \tag{5}$$

Similarly, the lateral cross-control derivative was estimated as:

$$C_{\mathcal{L}_{\delta_\mathrm{r}}} = \frac{C_{\mathcal{L}}(\beta = 0°, \delta_\mathrm{r}) - C_{\mathcal{L}}(\beta = \delta_\mathrm{r} = 0°)}{\delta_\mathrm{r}} . \tag{6}$$

The evaluation of the sideforce derivative $C_{Y_{\delta_\mathrm{r}}}$ is omitted, since Eqs. (5) and (6) directly provide the directional control and lateral cross-control powers. The aerodynamic curves are drawn in Fig. 15. As expected, the deflection of the rudder did not affect the slope of the curves, but provided their translation on the ordinate axis. A non-linear trend appeared at low sideslip angles and small rudder deflections, especially on the body-mounted configuration. The results of the application of Eqs. (5) and (6) are shown in Table 9. The directional control power for the body-mounted tail was about 10% larger than that of the T-tail. This was attributed to the larger surface of the former. The VeDSC method [27], by which these geometries were generated, guaranteed almost the same directional stability. The lateral cross-control power was very small, but stronger for the T-tail configuration.

From the data of the previous tables, the rudder effectiveness $\tau = \mathrm{d}\beta / \mathrm{d}\delta_\mathrm{r}$ was evaluated as:

$$\tau = \left| \frac{C_{\mathcal{N}_{\delta_\mathrm{r}}}}{C_{\mathcal{N}_\beta,\text{tail-on}} - C_{\mathcal{N}_\beta,\text{tail-off}}} \right|_{\beta=0^\circ}, \tag{7}$$

where the quantity at the denominator is an estimation of the vertical tail contribution to the directional stability derivative, $C_{\mathcal{N}_{\beta,\mathrm{V}}}$. For both tail configurations, the rudder effectiveness was about 0.53 at $\delta_\mathrm{r} = 10^\circ$ and 0.43 at $\delta_\mathrm{r} = 20^\circ$. The similar values between the two configurations indicate that both rudder control power $C_{\mathcal{N}_{\delta_\mathrm{r}}}$ and vertical tail contribution to directional stability $C_{\mathcal{N}_{\beta,\mathrm{V}}}$ are equally scaled despite the different tail layouts.

The aerodynamics of the rudder is a well-known topic, where the deflection of the directional control surface generates a local sideslip flow that generates a lower pressure, and hence a sideforce, on the vertical tail in the direction opposite to its rotation. Conversely, when the entire aircraft is in sideslip, the flowfield is completely different. Figure 16 shows the pressure distribution calculated with the numerical analyses for the above mentioned cases. Streamlines are also visible, highlighting the different paths of the flow particles around the vertical tail. As concerns the stability and control derivatives, the numerical results are in good agreement with wind tunnel data, with a difference of about 10%.

As concerns directional stability and control, a comment must be made on the equilibrium sideslip angles, which are found as the zero crossing of the $C_\mathcal{N}$ curves in Fig. 15b. For instance, at $\delta_\mathrm{r} = 20^\circ$, the value $\beta \approx 12^\circ$ can be found. This means that larger sideslip angles could not be sustained by either tail configurations. The rudder chord ratio of 25% appears insufficient to generate the necessary control power to keep the directional equilibrium in strong cross-wind conditions. This was initially attributed to the limited Reynolds number achievable in our wind tunnel, but numerical analyses have shown no significant differences between the results at Reynolds numbers of 0.4 million (wind tunnel value) and 7.5 million (possible full-scale value). Generally speaking, a figure of merit to assess directional controllability with respect to stability is the ratio between their derivatives. As a rule of thumb, it is appropriate that $C_{\mathcal{N}_\beta}/C_{\mathcal{N}_{\delta_\mathrm{r}}} < 1$ to achieve equilibrium at large sideslip angles. The aircraft model has a value of about 1.65, indicating an excessive directional stability with respect to rudder control power.

3.7 Combined effects of angles of attack and sideslip

The combined effects of the angles of attack α and sideslip β are shown in Fig. 17 for both WB and WBHV configurations. The model was investigated at $\alpha = 0^\circ$ and 5°. The sideforce coefficient was negligibly affected by the angle of attack. However, the moment coefficients were altered, indicating that the free couples on the wing-body were changed due to the combined effects of both attitude angles. The slope of the yawing moment curves changed so that the wing-body at $\alpha = 5^\circ$ was less unstable than at $\alpha = 0^\circ$, with the magnitude of $C_{\mathcal{N}_\beta}$ decreased by about 28%. Similarly, the complete aircraft with body-mounted tail (WBHVb) had the directional stability derivative increased by 11%. Conversely, $C_{\mathcal{N}_\beta}$ was practically unaffected on the T-tail configuration (WBHVt). References [13, 18, 46] did not observed significant changes of the yawing moment coefficient with the angle of attack.

As concerns the rolling moment, the WB combination became laterally unstable at low angles of sideslip and $\alpha = 5^\circ$. The dihedral effect due to the high-wing layout was lost. Lateral stability at low sideslip angles was reintroduced with the contribution of the empennage. The body-mounted horizontal plane slightly improved the situation, restoring a small negative value of $C_{\mathcal{L}_\beta}$. The T-tail configuration had certainly a larger beneficial effect at $\alpha = 5°$, but anyway lost some lateral stability with respect to the case at zero angle of attack, achieving values close to those of the body-mounted configuration at $\alpha = 0°$. References [13, 18] did not show effects of the angle of attack on the rolling moment coefficient.

Also other combinations were investigated at angle of attack, although their charts have not been reported for the sake of brevity. Test data were sufficient to estimate the vertical tail effectiveness (sidewash) at $\alpha = 5°$ with horizontal tail on. Table 10 reports the results of the application of Eqs. (2) and (4) and a comparison for the two angles of attack. Both approaches — with sideforce and with yawing moment coefficients — gave an increase of vertical tail effectiveness (reduction of sidewash effect) with the body-mounted tail at angle of attack. Conversely, a reduction was measured with the T-tail configuration.

3.8 Combined effects of flaps and angle of sideslip at different angles of attack

Three different flap deflections have been investigated: the clean configuration $\delta_\mathrm{f} = 0°$, the take-off configuration $\delta_\mathrm{f} = 15°$, and the landing configuration $\delta_\mathrm{f} = 30°$. Results have been reported in Fig. 18 for the WB combination and in Fig. 19 for the WBHV combination. The effects of flap were negligible on the sideforce coefficients for all the configurations and angles of attack.

The directional stability derivative was not significantly altered by the flap deflection, especially for the WB combination at low angles of sideslip. The angle of attack, as shown in the previous section, reduced the magnitude of directional instability of the wing-body. The complete aircraft has shown a similar behaviour, with the deflection of the flaps reducing the directional stability derivative at moderate and large angles of sideslip. At $\alpha = 5°$, the yawing moment coefficient curves were more linear than at $\alpha = 0°$. The yawing moment coefficient achieved larger values at higher attitudes and the body-mounted tail configuration performed best, as expected from the previous results.

Conversely, the deflection of the flaps counteracted the lateral stability of the high-wing layout, amplifying a behaviour that was highlighted in the previous section, i.e., that the wing-body and the complete aircraft with body-mounted tail at angle of attack were laterally unstable. The effect of the flap was to introduce a significant amount of lateral instability for both wing-body and complete aircraft. Even the T-tail configuration was affected, with poor lateral stability at low angles of sideslip for $\delta_\mathrm{f} = 0°$, mild and large instability for $\delta_\mathrm{f} = 15°$ and $\delta_\mathrm{f} = 30°$, respectively. This effect was not anticipated,

Table 8 Vertical tail effectiveness in sideslip

Application	Hor. tail off	Hor. tail on
Sideforce, Vb	0.845	0.864
Sideforce, Vt	0.862	0.818
Yawing moment, Vb	0.830	0.853
Yawing moment, Vt	0.849	0.811

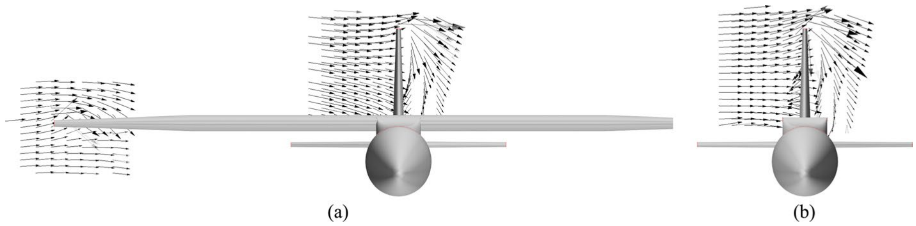

Fig. 14 Velocity vectors showing the wingtip vortex induction on the vertical tail in sideslip: **a** wing-on; **b** wing-off. The relative magnitude of the tailplane vectors has been increased for the sake of clarity

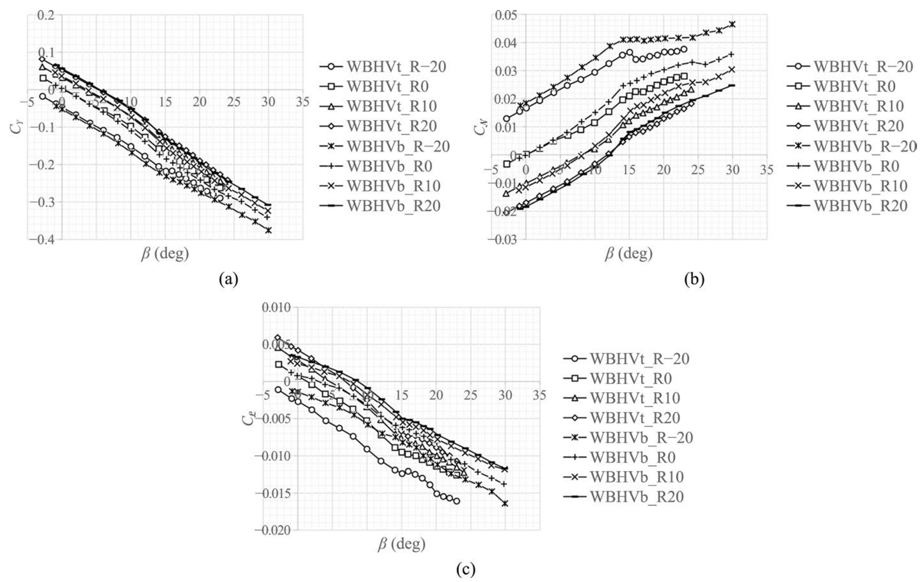

Fig. 15 Complete aircraft in sideslip with different rudder deflections: **a** sideforce coefficient; **b** yawing moment coefficient; **c** rolling moment coefficient

since the derivative $C_{\mathcal{L}_\beta}$ should not be severely affected for straight wings with flap deflected [12]. Test data have shown that lateral instability may arise also at large sideslip angles and the situation is expected to worsen at larger angles of attack, highlighting the necessity of a careful selection of the aircraft configuration layout, especially the effective dihedral for lateral control in critical situations, such as cross-wind landings. Tables 11 and 12 report the values of the aerodynamic derivatives for the configurations described in this section.

It may be argued that the detrimental results on the lateral stability were due to the chosen reference point, which is quite high with respect to the fuselage. For this reason, the rolling characteristics were evaluated again at different reference positions, as shown in Fig. 20. The first position is the reference point for the moments applied in the previous discussion. The other two are downward translations of the first one. The new evaluation has been done on the wing-body configuration at different flap deflections and angles of attack. Figure 21 shows that, despite the change of reference point position, the rolling characteristics with flap deflected were still unsatisfactory for most of the wind tunnel runs, with the $C_{\mathcal{L}_\beta}$ positive until $\beta \approx 8°$, and then a slope change followed. The specific cause of this behaviour is still unknown and it is worth of a dedicated investigation.

Once the reference point was removed as the probable cause of the unsatisfactory lateral stability of the aircraft model, numerical analyses were performed on the WB configurations at different flap deflections and angles of attack. Both the simulations and the previously presented wind tunnel data showed a decrease of lateral stability with increasing lift coefficient, for any combination of flap setting and angle of attack. Numerical and experimental values of the rolling moment coefficient derivative were in good agreement, diverging only at high values of the lift coefficient. These values were expected to be poorly affected by the lift force [18, 46].

A comparison has been made between the numerical and experimental data of the WB configuration discussed in this paper with those reported in Ref. [46] for a wing-body made up of an ellipsoid (slenderness ratio: 7) with a rectangular wing (aspect ratio: 5). Further details on this geometry are not available, so it was assumed that the rolling moment coefficient presented in [46] was normalized with the wing area and span and evaluated about the body symmetry axis. To make a fair comparison, results of our WB configuration were evaluated at reference point 2. Figure 22 shows the roll stability derivative vs. the lift coefficient for the above mentioned configurations. It appears that, despite the high-wing layout, our model had poor lateral stability even at low values of the lift coefficient. The effective dihedral generated by the relative wing-body position was insufficient.

The numerical simulation provided insights on the causes that led to the lateral instability of the configuration. In Fig 23, numerical results of the contributions of wing (and flaps where deployed) and fuselage to the rolling moment coefficient derivative are shown. Both increase with the lift coefficient. However, numerical simulations have also shown that the wing center of pressure, initially located on the upwind side of the wing at low values of the lift coefficient, moved towards the symmetry plane and to the downwind side of the wing with the increase of the lift coefficient. This has been attributed to the circulation of the flow on the wing that becomes much stronger than the effect of the lateral velocity component, restoring the symmetry of the aerodynamic loading and moving the resultant of the lift forces towards the downwind side. The wing loading has been represented with the distribution of pressure coefficient defined as:

Table 9 Stability and control derivatives at different rudder deflections. Derivatives in deg^{-1}

	Body-mounted tail				**T-tail**			
δ_r	**−20°**	**0°**	**10°**	**20°**	**−20°**	**0°**	**10°**	**20°**
$C_{\mathcal{N}_0}$	0.0184	0.0000	−0.0114	−0.0183	0.0167	0.0002	−0.0101	−0.0169
$C_{\mathcal{N}_\beta}$	0.0015	0.0013	0.0013	0.0013	0.0013	0.0012	0.0012	0.0013
$C_{\mathcal{N}_{\delta_\mathrm{r}}}$	−0.0009	n.a.	−0.0011	−0.0009	−0.0008	n.a.	−0.0010	−0.0009
$C_{\mathcal{L}_0}$	−0.0015	0.0009	0.0024	0.0033	−0.0027	0.0007	0.0028	0.0042
$C_{\mathcal{L}_\beta}$	−0.0004	−0.0003	−0.0003	−0.0004	−0.0006	−0.0006	−0.0006	−0.0006
$C_{\mathcal{L}_{\delta_\mathrm{r}}}$	0.0001	n.a.	0.0002	0.0001	0.0002	n.a.	0.0002	0.0002

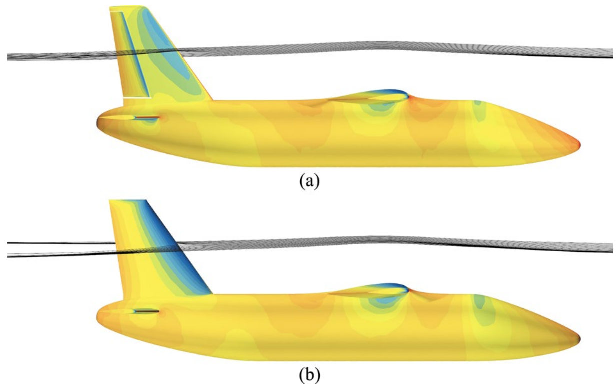

Fig. 16 Pressure distribution on the aircraft model: **a** with rudder deflected and no sideslip $\delta_r = 20°, \beta = 0°$; **b** without rudder deflected and the entire model in sideslip $\delta_r = 0°, \beta = -6°$

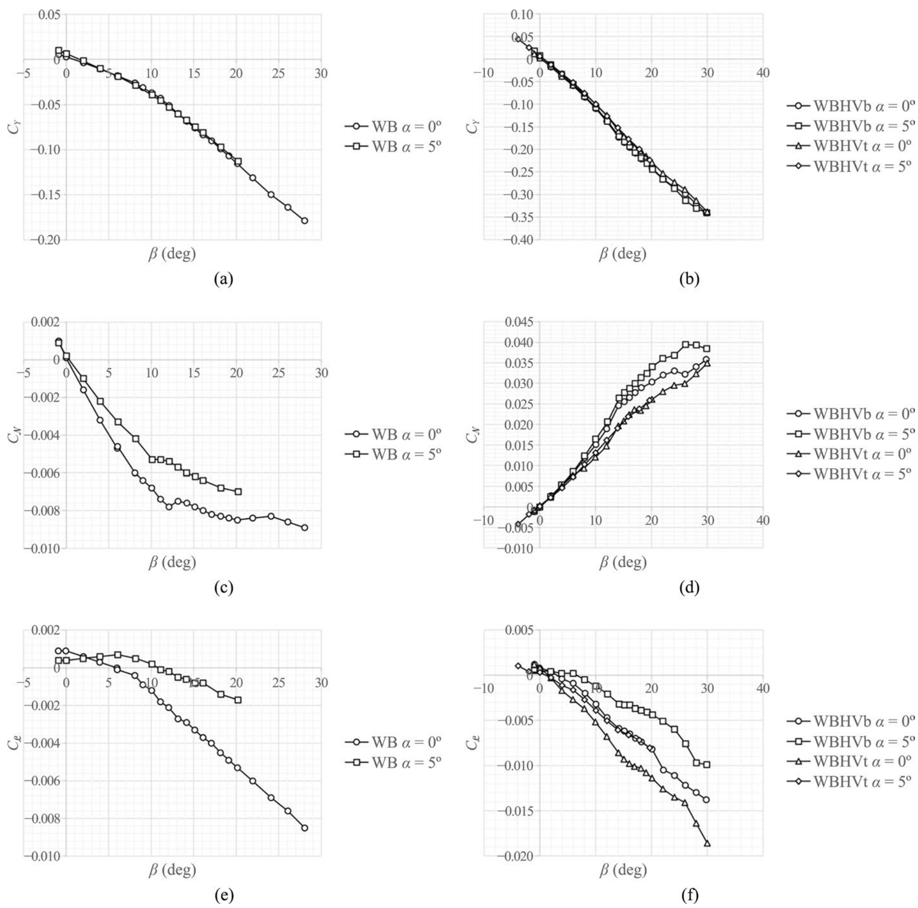

Fig. 17 Wing-body and complete aircraft in sideslip at different angles of attack: **a** WB sideforce coefficient; **b** WBHV sideforce coefficient; **c** WB yawing moment coefficient; **d** WBHV yawing moment coefficient; **e** WB rolling moment coefficient; **f** WBHV rolling moment coefficient

$$C_p = \frac{p - p_\infty}{q_\infty}, \tag{8}$$

Table 10 Vertical tail effectiveness in sideslip at two angles of attack and with horizontal tail on

Application	$\alpha = 0°$	$\alpha = 5°$
Sideforce, Vb	0.864	0.882
Sideforce, Vt	0.818	0.795
Yawing moment, Vb	0.853	0.855
Yawing moment, Vt	0.811	0.785

where p is the local value of the static pressure, whereas p_∞ and q_∞ are respectively the reference values of the static and dynamic pressure at the farfield. Figure 24 shows the C_p distributions on the WB configuration for the lowest and highest values of the lift coefficient, that is where the model had respectively the maximum and minimum lateral stability. The center of wing aerodynamic loads has also been indicated. Although its displacement was small, it can be observed that at high lift the center of loads moved backward and to the left.

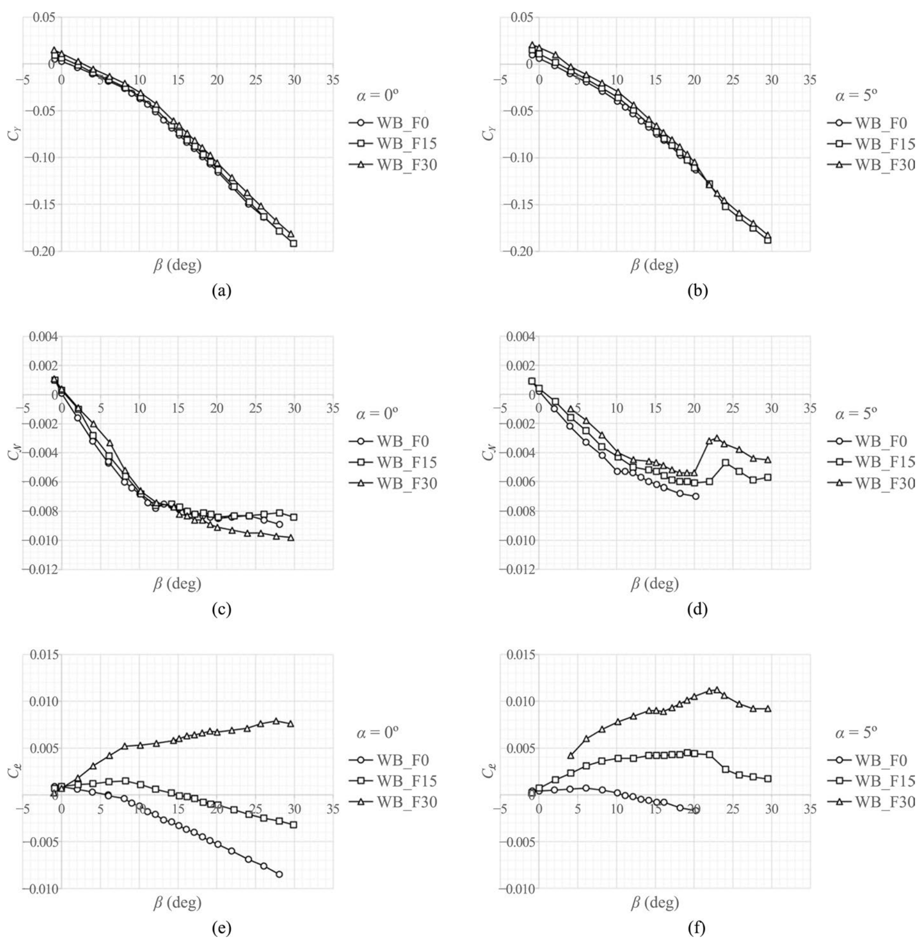

Fig. 18 Wing-body in sideslip at different angles of attack and flap deflections: **a** sideforce coefficient at $\alpha = 0°$; **b** sideforce coefficient at $\alpha = 5°$; **c** yawing moment coefficient at $\alpha = 0°$; **d** yawing moment coefficient at $\alpha = 5°$; **e** rolling moment coefficient at $\alpha = 0°$; **f** rolling moment coefficient at $\alpha = 5°$

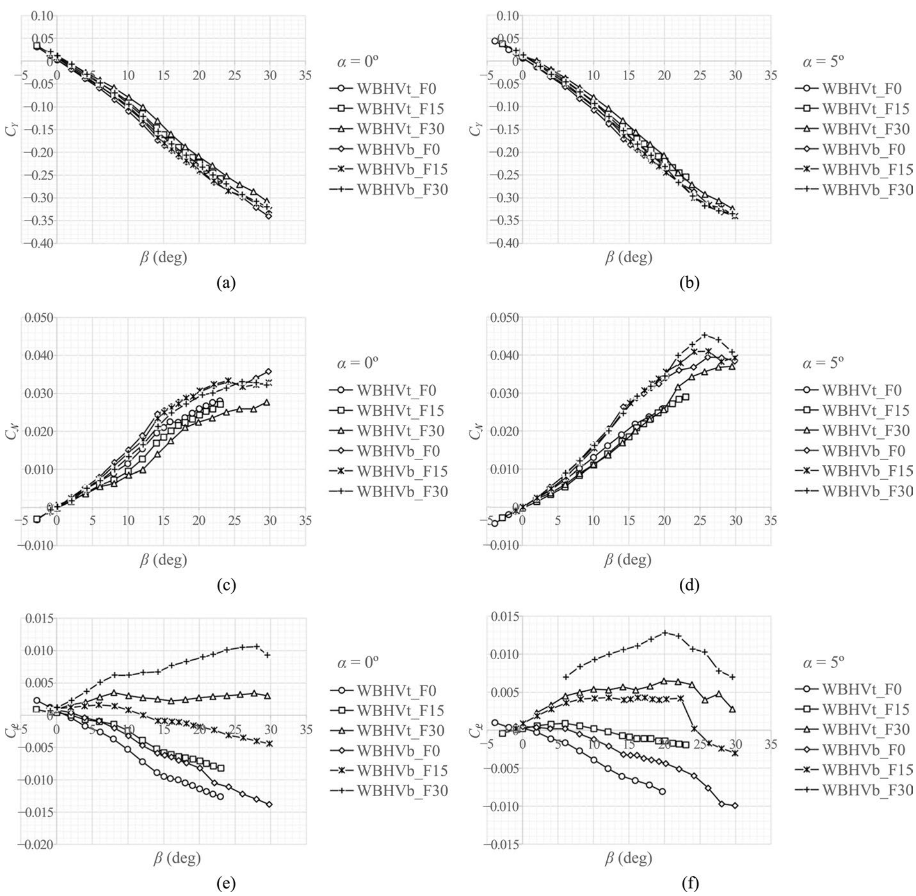

Fig. 19 Complete aircraft in sideslip at different angles of attack and flap deflections: **a** sideforce coefficient at $\alpha = 0°$; **b** sideforce coefficient at $\alpha = 5°$; **c** yawing moment coefficient at $\alpha = 0°$; **d** yawing moment coefficient at $\alpha = 5°$; **e**) rolling moment coefficient at $\alpha = 0°$; (**f**) rolling moment coefficient at $\alpha = 5°$

To further highlight the contribution of each component to the rolling moment, the $C_{\mathcal{L}}$ distribution function has been defined as follows:

$$f(C_{\mathcal{L}}) = \frac{[(\mathbf{r} - \mathbf{r_0}) \times (\mathbf{f_p} + \mathbf{f_s})] \cdot \mathbf{x}}{\frac{1}{2}\rho_\infty V_\infty^2 Sb}, \tag{9}$$

where $\mathbf{r} - \mathbf{r_0}$ is the position vector of a cell of the numerical domain in the selected coordinate system (body reference frame), $\mathbf{f_p}$ is the force vector due to the pressure, $\mathbf{f_s}$ is the force vector due to the shear, and $\mathbf{x}$ is the direction of the x-axis in the body reference

Table 11 Directional stability derivative $C_{\mathcal{N}_\beta}$ at different flap deflections and angles of attack. Derivatives in deg^{-1}

	$\alpha = 0°$			$\alpha = 5°$		
δ_f	0°	15°	30°	0°	15°	30°
WB	–0.00078	–0.00073	–0.00066	–0.00056	–0.00050	–0.00045
WBHVb	0.00134	0.00129	0.00118	0.00148	0.00137	0.00147
WBHVt	0.00122	0.00096	0.00073	0.00119	0.00099	0.00111

Table 12 Lateral stability derivative $C_{\mathcal{L}_\beta}$ at different flap deflections and angles of attack. Derivatives in deg^{-1}

	$\alpha = 0°$			$\alpha = 5°$		
δ_f	0°	15°	30°	0°	15°	30°
WB	–0.00015	0.00008	0.00056	0.00002	0.00038	0.00069
WBHVb	–0.00030	0.00008	0.00062	–0.00010	0.00043	0.00115
WBHVt	–0.00058	–0.00022	0.00031	–0.00030	0.00010	0.00046

frame. At the denominator there are the usual normalization quantities. Such function has been applied at each cell of the WB numerical model to get the distributions illustrated in Fig. 25. The rolling moment coefficient calculated in the numerical simulations is simply:

$$C_{\mathcal{L}} = \sum_i^n f(C_{\mathcal{L}}),$$

that is the sum of the contributions of each cell of the wing-body boundaries. In Fig. 25, cold colors represent negative values of the $f(C_{\mathcal{L}})$ function, and that is a contribution to roll to the left. Conversely, warm colors represent a contribution to roll to the right. Observe that at low values of the lift coefficient there is a blue predominance on the wing, meaning that its contribution to roll is stable. At high values of the lift coefficient, it is difficult to infer the lateral stability from the contour scene, as both half-wings provide almost equal and opposite contributions. The figure also shows the contribution of the fuselage, with the green and yellow colors representing the tendency to roll to the left and to the right, respectively. The center of wing aerodynamic loads has also been indicated. In this figure, it is apparent that at high lift, it is much closer to the symmetry plane than at low lift.

Numerical analyses have shown that the magnitudes of the contribution of each half-wing to the rolling moment were about 49% and 51% for the left (downwind) and right (upwind) sides, respectively, for low values of the lift coefficient. At the highest value, these proportions reversed to about 50.1% and 49.9% for the left and right sides, respectively. Although these contributions are practically equal and opposite, the tendency of the wing to achieve a symmetrical load and the increasing lateral instability of the

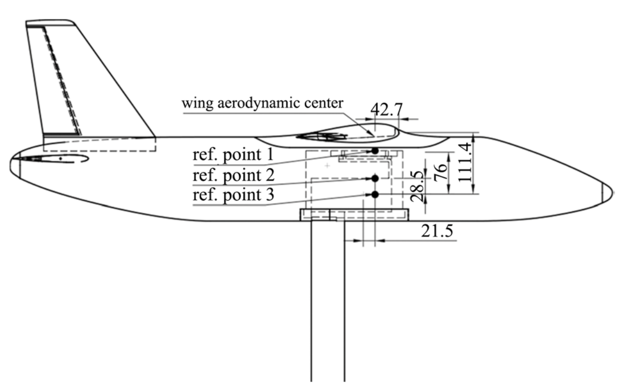

Fig. 20 Locations of reference points for the evaluation of rolling moment. Units in mm

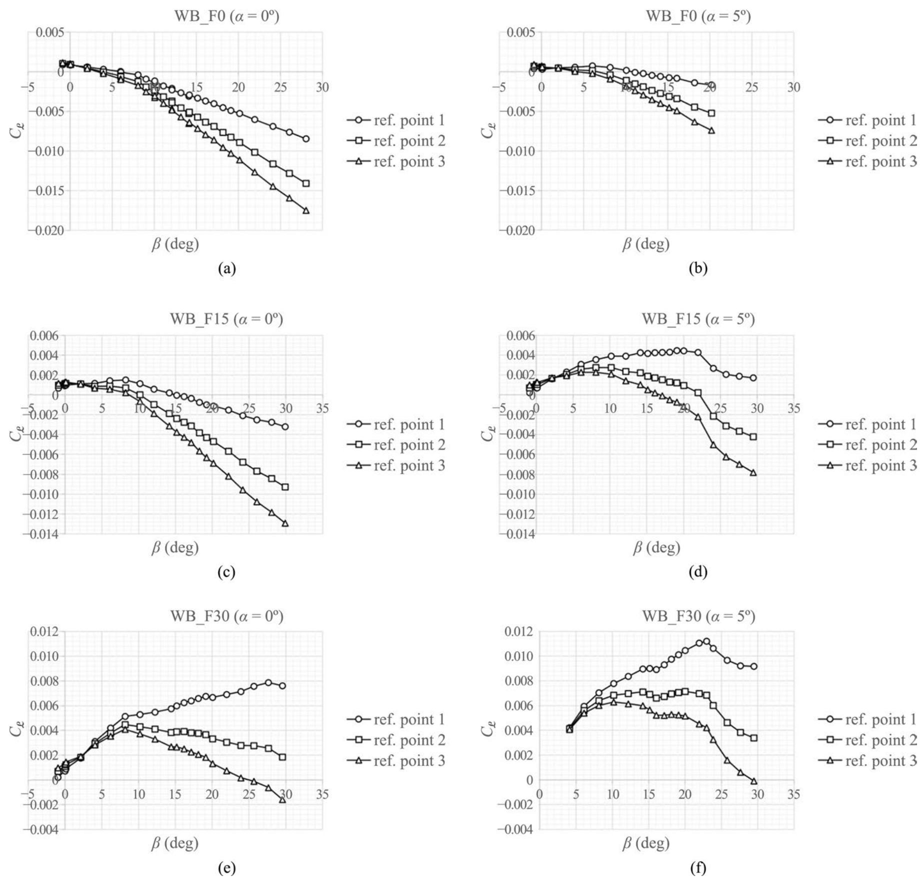

Fig. 21 Comparison of wing-body rolling moment coefficient curves at different flap deflections and angles of attack: **a** $\delta_f = 0°$ and $\alpha = 0°$; **b** $\delta_f = 0°$ and $\alpha = 5°$; **c** $\delta_f = 15°$ and $\alpha = 0°$; **d** $\delta_f = 15°$ and $\alpha = 5°$; **e** $\delta_f = 30°$ and $\alpha = 0°$; **f** $\delta_f = 30°$ and $\alpha = 5°$

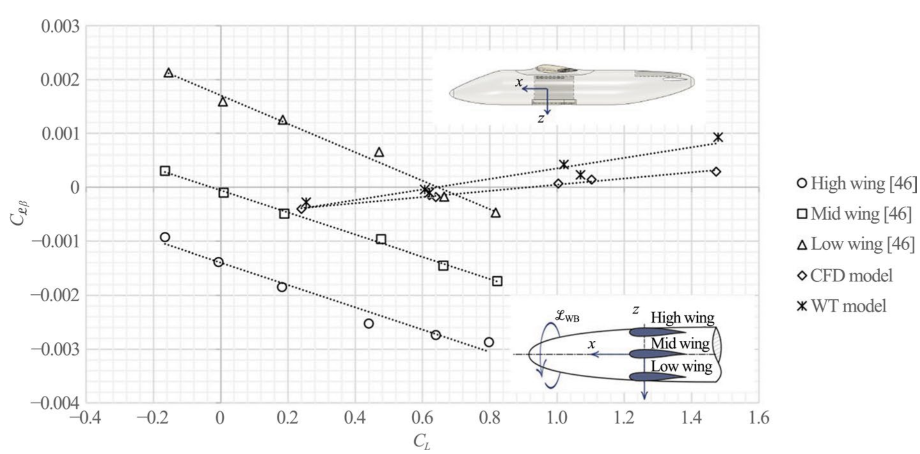

Fig. 22 Comparison of wing-body roll stability between literature, simulation, and test data. Ordinate values in deg^{-1}. The values of the first three datasets were derived from [46]

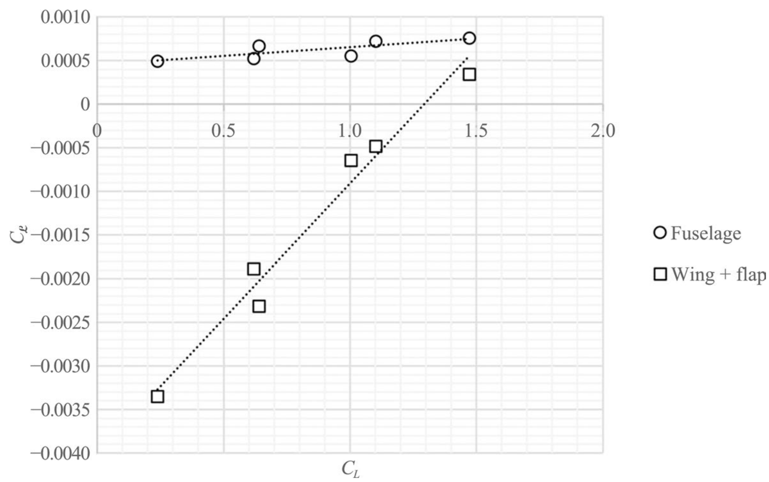

Fig. 23 Comparison of fuselage and wing contributions to the rolling moment coefficient of the WB configuration. Results from numerical analyses at $\beta = 6°$

fuselage made the WB configuration unstable to roll in high-lift conditions. Figure 26 shows the tangential velocity distribution on a cross-sectional plane located ahead of the wing and close to its leading edge. It is apparent that the effect of the wing upwash in high-lift conditions appears to be stronger than the cross-flow to the sideslip angle. This may explain the restoring symmetry of the wing load.

Since the high-wing layout was not sufficient to ensure the lateral stability of the aircraft configuration, in contradiction with the literature results that provide opposite trends with the lift coefficient, it is advisable to investigate with high-fidelity methods the static stability characteristics of any aircraft before freezing the configuration and go with the detail design. In this case, if the model were a specific aircraft and not a representative geometry, the solution could be adding a dihedral angle to the wing to achieve the desired lateral stability. From an academic point of view, these results may promote a systematic investigation on similar configurations that include the effects of fuselage shape, wing planform, wing-body relative position, and wing-body fillets.

4 Conclusions

The lateral-directional stability and control characteristics of the unpowered scaled model of the PROSIB 19-passenger aircraft have been investigated. The aircraft model had a classic tube-and-wing layout with a belly pod simulating a battery pack.

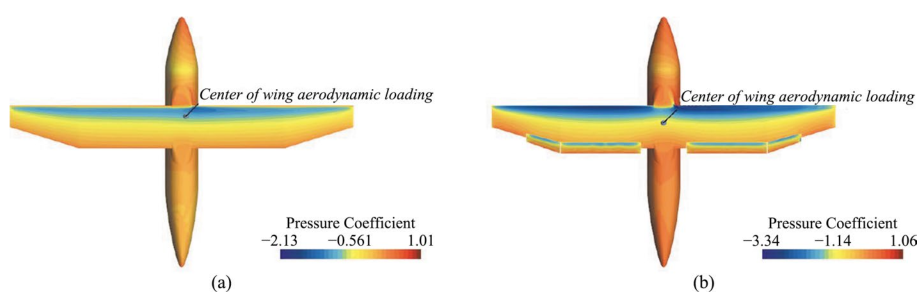

Fig. 24 Comparison of pressure coefficient contours at $\beta = 6°$ (lateral velocity component from the right): **a** $\alpha = 0°, \delta_f = 0°, C_L = 0.24$; **b** $\alpha = 5°, \delta_f = 30°, C_L = 1.47$

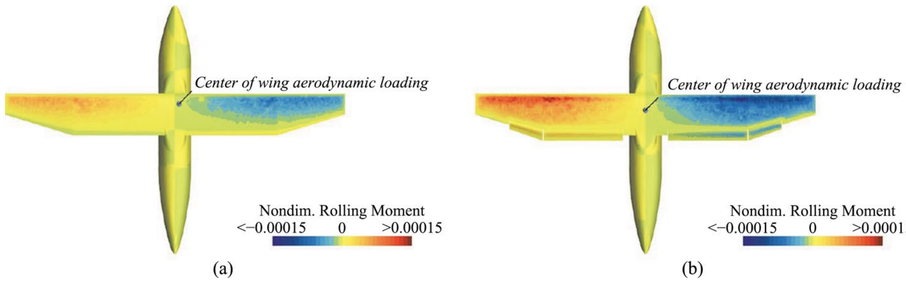

Fig. 25 Comparison of contours of the rolling moment contributions at $\beta = 6°$ (lateral velocity component from the right): **a** $\alpha = 0°, \delta_f = 0°, C_L = 0.24$; **b** $\alpha = 5°, \delta_f = 30°, C_L = 1.47$

Two tailplane configurations — a body mounted horizontal plane and a T-tail — have been tested to provide design guidelines on stability and control of small air transport airplanes. The wind tunnel runs were organized to extract data on the aerodynamic interference among the aircraft components. Wing-off, wing-body, and wing-body-tail combinations were investigated to estimate static stability derivatives and vertical tail effectiveness in sideslip (sidewash). The rudder was deflected at different angles to evaluate its control power and effectiveness. Numerical analyses were added to highlight aerodynamic interference effects that were not possible to capture with the experimental measurements.

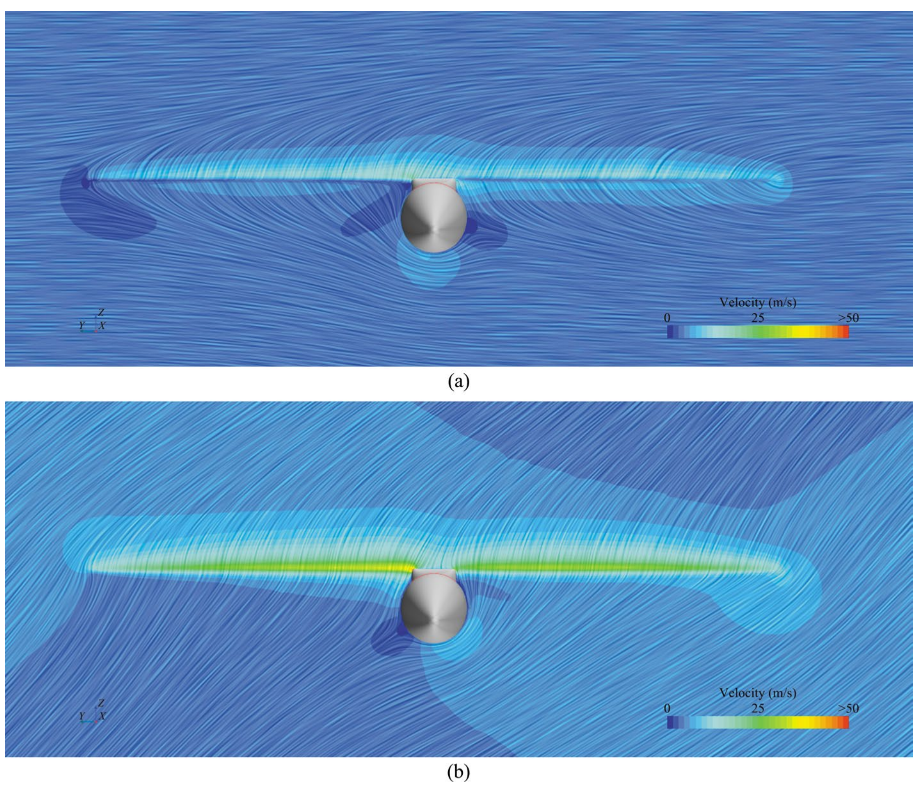

Fig. 26 Comparison of the tangential velocity at $\beta = 6°$ on a transverse plane located immediately ahead of the wing leading edge: **a** $\alpha = 0°, \delta_f = 0°, C_L = 0.24$; **b** $\alpha = 5°, \delta_f = 30°, C_L = 1.47$. Front view, lateral velocity component from the left

The wind tunnel runs of the clean configurations at zero angle of attack confirmed the lateral-directional static stability of the airplane model. The body-mounted tailplane performed slightly better in directional control and slightly worse in lateral stability than the T-tail configuration. Directional stability was essentially the same for both tailplanes, as expected from the authors' method. These characteristics were amplified at angle of attack, meaning that stable combinations were more stable and unstable combinations were more unstable. Conversely, the flap deflection reduced the lateral and directional stability characteristics for all the configurations. Combined effects of sideslip, angle of attack, and flap deflection highlighted a poor lateral stability of both empennage layouts. The detrimental effect of the flaps on lateral stability was particularly strong for the body-mounted tail configuration, raising the attention on the unexpected results and promoting a careful selection and validation of the entire aircraft configuration layout. These results are not predicted in the literature, especially in the semi-empirical methods for preliminary aircraft design and analysis, where the effect of the angle of attack on the lateral and directional stability derivative is ignored. Further data processing highlighted that the detrimental effect of flap deflection on lateral stability was not due to the position of the moments' reference point, but rather to the wing circulation that at high lift moved the center of the aerodynamic loading towards the downwind side, while the fuselage roll instability increased with the lift coefficient.

Numerical analyses have also shown how the aerodynamics of the configuration influenced the generation of forces and moments, highlighting the role of wingtip vortices on the sidewash effect and confirming the directional control characteristics of the model. As concerns the belly-mounted pod, it unexpectedly reduced the wing-body directional instability, while it was neutral on the lateral stability. This behavior was not confirmed by the numerical analyses, which provided an opposite trend. The specific cause has been attributed to an aerodynamic interference effect that was not predicted by the simulations, although caution must be taken in considering the wind tunnel data on the pod as completely valid. This is a limitation of our investigation that could be overcome by repeating the test with a different system of measurement.

In conclusion, the results presented in this paper established a dataset of power-off aerodynamic derivatives for the PROSIB 19-passenger wind tunnel model, highlighted the characteristics of two opposite tailplane layouts, and provided insights on the effects of aerodynamic interference on a typical SAT configuration. It is the authors' opinion that the discussion and the results will be useful to researchers working on similar aircraft configurations.

Abbreviations

ACARE	Advisory Council for Aviation Research and Innovation in Europe
CNC	Computerized Numerical Control
DATCOM	Data Compendium
NACA	National Advisory Committee for Aeronautics
NASA	National Aeronautics and Space Administration
SAT	Small Air Transport
USAF	United States Air Force
VeDSC	Vertical tail Design, Stability, and Control

Acknowledgements
The authors are grateful to Eng. Giuseppe Buonagura for his help with the wind tunnel runs and data acquisition.

Authors' contributions

All authors contributed to the study conception and design. Material preparation, data collection and analysis were performed by Danilo Ciliberti and Fabrizio Nicolosi. The first draft of the manuscript was written by Danilo Ciliberti and all authors commented on previous versions of the manuscript. The revision was cured by Danilo Ciliberti and supervised by Fabrizio Nicolosi. All authors read and approved the final manuscript.

Funding

This research was funded by the Italian PROSIB (Propulsione e Sistemi Ibridi per velivoli ad ala fissa e rotante—Hybrid Propulsion and Systems for fixed and rotary wing aircraft) project PNR 2015-2020 ARS01_00297 led by Leonardo S.p.A.

Availability of data and materials

All data generated or analysed during this study are included in this published article.

Declarations

Competing interests

The authors have no financial or proprietary interests in any material discussed in this article.

Received: 26 June 2024 Accepted: 1 September 2024

Published online: 28 February 2025

References

1. ICAO (2019) Guidance on the development of states' action plans on CO_2 emissions reduction activities. International Civil Aviation Organization, Montréal
2. National Academies of Sciences, Engineering and Medicine (2016) Commercial aircraft propulsion and energy systems research: Reducing global carbon emissions. The National Academies Press, Washington DC. https://doi.org/10.17226/23490
3. Moore MD, Fredericks B (2014) Misconceptions of electric propulsion aircraft and their emergent aviation markets. In: 52nd aerospace sciences meeting, National Harbor, 13–17 January 2014. https://doi.org/10.2514/6.2014-0535
4. Dannier A, Del Pizzo A, Di Noia LP et al (2018) Sizing procedure of PMSMs for hybrid parallel aircraft propulsion. In: 2018 IEEE international conference on electrical systems for aircraft, railway, ship propulsion and road vehicles & international transportation electrification conference (ESARS-ITEC), Nottingham, 7–9 November 2018. https://doi.org/10.1109/ESARS-ITEC.2018.8607709
5. Bocii LS, Di Noia LP, Rizzo R (2019) Optimization of the energy storage of series-hybrid propelled aircraft by means of integer differential evolution. Aerospace 6(5):59. https://doi.org/10.3390/aerospace6050059
6. Nicolosi F, Marciello V, Cusati V et al (2022) Technology roadmap and conceptual design of hybrid and electric-configurations in the commuter class. In: 33rd congress of the international council of the aeronautical sciences, Stockholm, 4-9 September 2022
7. Orefice F, Della Vecchia P, Ciliberti D et al (2021) Preliminary design to fulfil future market demand of electric aircraft. Int Rev Aerosp Eng 14(6):294–308. https://doi.org/10.15866/irease.v14i6.20814
8. Ciliberti D, Buonagura G, Nicolosi F (2023) Longitudinal wind tunnel tests of the PROSIB 19-pax airplane. Appl Sci 13(21):11928. https://doi.org/10.3390/app132111928
9. European Commission (2011) Flightpath 2050 – Europe's vision for aviation: maintaining global leadership and serving society's needs. Publications Office of the European Union, Belgium
10. Advisory Council for Aeronautics Research in Europe (2008) 2008 addendum to the strategic research agenda. Advisory Council for Aviation Research and Innovation in Europe, Brussels
11. Ciliberti D, Della Vecchia P, Memmolo V et al (2022) The enabling technologies for a quasi-zero emissions commuter aircraft. Aerospace 9(6):319. https://doi.org/10.3390/aerospace9060319
12. Perkins CD, Hage RE (1949) Airplane performance stability and control. Wiley, New York
13. Finck RD (1978) USAF stability and control Datcom. Wright-Patterson Air Force Base, Dayton
14. ESDU Technical Committees (1982) Contribution of fin to sideforce, yawing moment and rolling moment derivatives due to sideslip, $(Y_v)_F$, $(N_v)_F$, $(L_v)_F$, in the presence of body, wing and tailplane (ESDU 82010). Engineering Sciences Data Unit, London
15. Pass HR (1940) Analysis of wind-tunnel data on directional stability and control (NACA-TN-775). National Advisory Committee for Aeronautics, Washington DC
16. Sears RI (1943) Wind-tunnel data on the aerodynamic characteristics of airplane control surfaces (NACA-WR-L-663). National Advisory Committee for Aeronautics, Washington DC
17. Kayten GG, Koven W (1945) Comparison of wind-tunnel and flight measurements of stability and control characteristics of a Douglas A-26 airplane (NACA-TR-816). National Advisory Committee for Aeronautics, Washington DC
18. Bamber MJ, House RO (1939) Wind-tunnel investigation of effect of yaw on lateral-stability characteristics II - rectangular NACA 23012 wing with a circular fuselage and a fin (NACA-TN-730). National Advisory Committee for Aeronautics, Washington DC
19. House RO, Wallace AR (1941) Wind-tunnel investigation of effect of interference on lateral-stability characteristics of four NACA 23012 wings, an elliptical and circular fuselage and vertical fins (NACA-TR-705). National Advisory Committee for Aeronautics, Washington DC
20. Murray HE (1946) Wind-tunnel investigation of end-plate effects of horizontal tails on a vertical tail compared with available theory (NACA-TN-1050). National Advisory Committee for Aeronautics, Washington DC

21. Brewer JD, Lichtenstein JH (1950) Effect of horizontal tail on low-speed static lateral stability characteristics of a model having 45° sweptback wing and tail surfaces (NACA-TN-2010). National Advisory Committee for Aeronautics, Washington DC
22. Queijo MJ, Wolhart WD (1951) Experimental investigation of the effect of vertical-tail size and length and of fuselage shape and length on the static lateral stability characteristics of a model with 45° sweptback wing and tail surfaces (NACA-TR-1049). National Advisory Committee for Aeronautics, Washington DC
23. Goodman A (1951) Effects of wing position and horizontal-tail position on the static stability characteristics of models with unswept and 45° sweptback surfaces with some reference to mutual interference (NACA-TN-2504). National Advisory Committee for Aeronautics, Washington DC
24. Recant IG, Swanson RS (1942) Determination of the stability and control characteristics of airplanes from tests of powered models (NACA-WR-L-710). National Advisory Committee for Aeronautics, Washington DC
25. Garner HC, Rogers EWE, Acum WEA et al (1966) Subsonic wind tunnel wall corrections. North Atlantic Treaty Organization, Paris
26. Barlow JB, Rae WH, Pope A (1999) Low-speed wind tunnel testing, 3rd edn. Wiley, New York
27. Ciliberti D, Della Vecchia P, Nicolosi F et al (2017) Aircraft directional stability and vertical tail design: A review of semi-empirical methods. Prog Aerosp Sci 95:140–172. https://doi.org/10.1016/j.paerosci.2017.11.001
28. Nicolosi F, Ciliberti D, Della Vecchia P et al (2018) Wind tunnel testing of a generic regional turboprop aircraft modular model and development of improved design guidelines. In: 2018 applied aerodynamics conference, 25–29 June 2018, Reston. https://doi.org/10.2514/6.2018-2855
29. Damljanović D, Vuković Đ, Ocokoljić G et al (2021) Wind tunnel testing of ONERA-M, AGARD-B and HB-2 standard models at off-design conditions. Aerospace 8(10):275. https://doi.org/10.3390/aerospace8100275
30. Katzoff S, Finn RS (1946) Effects of external fuel tanks and bombs on critical speeds of aircraft (NACA-WR-L-726). National Advisory Committee for Aeronautics, Washington DC
31. Morris OA (1957) Aerodynamic forces and moments on a large ogive-cylinder store at various locations below the fuselage center line of a swept-wing bomber configuration at a Mach number of 1.61 (NACA-RM-L56I25). National Advisory Committee for Aeronautics, Washington DC
32. Spearman ML (1972) Some effects of external stores on the static stability of fighter airplanes (NASA-TN-D-6775). National Aeronautics and Space Administration, Washington DC
33. Heart Aerospace (2023) Learn more about the ES-30. https://heartaerospace.com/es-30/. Accessed 13 Oct 2023
34. Ampaire Inc (2023) Meet the eco caravan. https://www.ampaire.com/vehicles/eco-caravan. Accessed 13 Oct 2023
35. Shelton DB (2009) Removable cargo pod with lifting mechanism and open top. US Patent 8128026-B2, 15 Jan 2009
36. Moonan WC (2010) Evaluation of the aerodynamics of an aircraft fuselage pod using analytical, CFD, and flight testing techniques. Dissertation, University of Tennessee
37. Silverstein A, Katzoff S (1939) Design charts for predicting downwash angles and wake characteristics behind plain and flapped wings (NACA-TR-648). National Advisory Commitee for Aeronautics, Washington DC
38. Spreemann KP (1959) Design guide for pitch-up evaluation and investigation at high subsonic speeds of possible limitations due to wing-aspect-ratio variations (NASA-TM-X-26). National Aeronautics and Space Administration, Washington DC
39. Recant IG, Wallace AR (1941) Wind tunnel investigation of the effect of vertical position of the wing on the side flow in the region of the vertical tail (NACA-TN-804). National Advisory Committee for Aeronautics, Washington DC
40. Goodman A, Thomas DF Jr (1954) Effects of wing position and fuselage size on the low-speed static and rolling stability characteristics of a delta-wing model (NACA-TR-1224). National Advisory Committee for Aeronautics, Washington DC
41. Letko W (1956) Experimental investigation at low speed of the effects of wing position on the static stability of models having fuselages of various cross sections and unswept and 45°sweptback surfaces (NACA-TN-3857). National Advisory Committee for Aeronautics, Washington DC
42. Wiggins JW, Kuhn RE, Fournier PG (1956) Wind-tunnel investigation to determine the horizontal- and vertical-tail contributions to the static lateral stability characteristics of a complete-model swept-wing configuration at high subsonic speeds (NACA-TN-3818). National Advisory Committee for Aeronautics, Washington DC
43. Jaquet BM, Fletcher HS (1957) Effects of fuselage nose length and a canopy on the static longitudinal and lateral stability characteristics of 45°sweptback airplane models having fuselages with square cross sections (NACA-TN-3961). National Advisory Committee for Aeronautics, Washington DC
44. Della Vecchia P, Nicolosi F, Ciliberti D (2015) Aircraft directional stability prediction method by CFD. In: 33rd AIAA applied aerodynamics conference, Reston, 22-26 June 2015. https://doi.org/10.2514/6.2015-2255
45. Multhopp H (1942) Aerodynamics of the fuselage (NACA-TM-1036). National Advisory Committee for Aeronautics, Washington DC
46. Schlichting H, Truckenbrodt E (1979) Aerodynamics of the airplane, 2nd edn. McGraw-Hill, New York